Integrative study of mitochondrial dysfunction in skeletal muscle during pancreatic cancer cachexia

Tristan Gicquel[1,2], Fabio Marchiano[3], Gabriela Reyes-Castellanos[1,2], Stéphane Audebert[1], Luc Camoin[1], Bianca Habermann[3], Benoit Giannesini[4], Alice Carrier[1,2]*

Affiliations:

[1] Aix Marseille Univ, Inserm, CNRS, Institut Paoli-Calmettes, Centre de Recherche en Cancérologie de Marseille (CRCM), Marseille, France

[2]French Network for Nutrition and Cancer Research (NACRe network), Jouy-en-Josas, France.

[3]Aix Marseille Univ, CNRS, IBDM UMR7288, Marseille, France

[4]Aix Marseille Univ, CNRS, Centre de Résonance Magnétique Biologique et Médicale (CRMBM), Marseille, France

*To whom correspondence should be addressed: Alice Carrier, Centre de Recherche en Cancérologie de Marseille (CRCM), Campus de Luminy Case 915, 163 Avenue de Luminy, 13288 Marseille Cedex 9, France. Phone: +33 491828829 ; Fax : +33 491826083. Email: alice.carrier@inserm.fr.

ABSTRACT

Background:

Pancreatic Ductal AdenoCarcinoma (PDAC), the most frequent pancreatic cancer, is a deadly cancer since often diagnosed late and resistant to current therapies. A high proportion of PDAC patients are affected by cachexia induced by the tumor. This cachexia, characterized by loss of muscle mass and strength, contributes to patient frailty and poor therapeutic response. We showed that mitochondrial metabolism is reprogrammed in PDAC tumors and constitutes a vulnerability, opening novel therapeutic avenues. The objective of the present work was to investigate the molecular mechanisms underlying mitochondrial remodeling in PDAC cachectic skeletal muscle.

Methods:

Our study focused on the gastrocnemius muscle of genetically-engineered mice developing spontaneously a PDAC associated with cachexia (KIC GEMM). We compared KIC mice developing a pancreatic tumor in 9-10 weeks to control littermates. We did an integrative study combining *in vivo* functional analyses by non-invasive Magnetic Resonance, and *ex-vivo* histology, Seahorse, RNA-sequencing, and proteomic mass spectrometry and western blotting analyses.

Results:

The cachectic KIC PDAC mice show a severe sarcopenia with loss of muscle mass and strength associated with reduced muscle fiber's size and induction of protein degradation processes. Mitochondria in PDAC atrophic muscles show decreased respiratory capacities and structural alterations, associated with deregulation of oxidative phosphorylation and mitochondrial dynamics pathways at the molecular level. Increased expression of multiple reactive oxygen species (ROS) defense genes suggests oxidative stress prone to affect mitochondrial macromolecules and homeostasis. Interestingly, multiple genes and proteins involved in DNA metabolism pathways, such as DNA damage, degradation of DNA, nucleotide synthesis, and folate pathway were found altered in sarcopenic mitochondria. While the number of mitochondria was not changed per cell, the mitochondrial mass was decreased by a factor of 2

and the mitochondrial DNA by a factor of 3, suggesting a defect in mitochondrial genome homeostasis.

Conclusions

We unveiled that mitochondrial alterations in skeletal muscle play a central role in PDAC-induced cachexia. Muscle atrophy is associated with strong mitochondrial metabolic defects that are not limited to carbohydrates and protein, but concern also lipids, ROS and nucleic acids. Our data provide a reference framework to guide towards the most relevant molecular markers that would be affected at the start of tumor development and could be targets in the clinic to limit PDAC-induced cachexia at early stages of the pathology.

Keywords: Pancreatic cancer, cachexia, muscle wasting, energetic metabolism, mitochondria.

INTRODUCTION

Pancreatic Ductal Adenocarcinoma (PDAC) accounts for 90% of pancreatic cancers with a very poor prognosis and one of the lowest 5-year relative survival rate (9%). It is the fourth-leading cause of cancer deaths, and predicted to become the second by 2030 as its incidence is rising [1-4]. The poor prognosis of PDAC is linked to a high percentage of locally advanced or metastatic diseases at the time of diagnosis, and the limited effectiveness of anti-tumor treatments, including immunotherapy [5]. This situation reflects the slow progress against this disease due to a lack of early diagnosis and major treatment advances.

Cancer-induced cachexia is a frequent debilitating muscle-wasting syndrome [6]. Cancer cachexia is characterized by lean body mass loss, muscle and adipose tissues loss, altered body metabolism, and inflammation. It is often irreversible and a sure sign of increased mortality and morbidity [7, 8]. More than 80% of PDAC patients are cachectic at the time of diagnosis, having lost body weight due to melting of metabolic organs, adipose tissue and muscles, induced by the presence of the tumor [9]. Tumor-induced cachexia, combining loss of muscle mass and strength, contributes significantly to the overall weakness of patients which hinders their clinical management and increases morbidity and mortality [10]. In this context, the limitation of patients' cachexia through nutritional support - diet and physical activity - is an approach increasingly developed in cancer hospitals. However, the development of nutritional strategies is limited by the poor knowledge of the mechanisms linking nutrition, cachexia and cancer. In addition, the knowledge of biomarkers to identify the patients that would benefit from nutritional strategies is required.

Exploration of the mechanisms underlying muscle wasting (sarcopenia) is done mostly in the aging context, nevertheless some insights were obtained in the recent years in cancer [6, 11-14]. As in aging, the main mechanism underlying cancer muscle wasting is alterations in amino acid and protein metabolism, comprising increased muscle protein degradation (proteolysis) and impaired muscle protein synthesis. The systemic inflammatory response induced by the tumor is one of the cancer characteristics promoting the activation of protein catabolism in skeletal muscle. Dysfunction of mitochondria also contributes to changes in muscle metabolism in cancer-induced

cachexia [15]. As the energy powerhouses of cells, mitochondria are instrumental in body organs homeostasis and function in general, and in skeletal muscle in particular since contraction to assure mobility is highly energy consuming. Beyond ATP production, mitochondria are a hub in nutrients metabolism, cell signaling and cell death, thus controlling cell life-death balance. Dysfunctional mitochondria are observed in many pathologies that are not restricted to muscular diseases [16-18].

Despite the central role of mitochondria in the physiopathology of skeletal muscle, their involvement in PDAC-induced muscle wasting was poorly addressed to date. Their role in cancers gained increased attention during the last decade, with the now-well admitted demonstration of their key role in cancer cell metabolic reprogramming, aberrant proliferation, survival, and resistance to therapies. Our laboratory showed that mitochondrial metabolism is reprogrammed in PDAC tumor cells and constitutes a vulnerability opening novel therapeutic avenues [19-21]. Nevertheless, mitochondria still have to be explored in the PDAC microenvironment and distant metabolic organs. Inflammation in skeletal muscle is a common feature observed in PDAC mouse models [22-24]. We thus made the hypothesis that the chronic inflammatory state induced by the pancreatic tumor could impact on skeletal muscle potentially through mitochondrial stress and dysfunction.

The objective of the present preclinical study was to investigate the mitochondrial remodeling in PDAC muscle, and decipher the underlying molecular mechanisms. Our study focused on the gastrocnemius muscle of genetically-engineered mice developing spontaneously a PDAC associated with cachexia, by implementing different technical approaches to provide a comprehensive description of PDAC-associated mitochondrial features in sarcopenic muscle. This study led to the demonstration of profound alterations of mitochondrial function, structure and gene expression in PDAC muscle, that could be used in the future to identify new PDAC-associated cachexia biomarkers.

RESULTS

The sarcopenia is severe in cachectic KIC PDAC mice

The preclinical model that we used was a genetically-engineered mouse model (GEMM) that develops spontaneously a PDAC and associated cachexia within nine to eleven weeks of age: the KIC mice in which the constitutively active mutant Kras oncogene is expressed and the tumor suppressor Ink4a is deleted, specifically in the pancreas (LSL-Kras^{G12D};Ink4a/Arf$^{lox/lox}$;Pdx1-Cre). Our study focused on the gastrocnemius skeletal muscle of male mice, via several technical approaches shown in Figure 1A (noninvasive multimodal MR *in vivo*, and oxygraphy, microscopy [visible, fluorescence, and transmission electron], RNA sequencing and protein mass spectrometry *ex vivo*).

KIC and control mice were sacrificed and analyzed at the age when the KIC showed signs of disease, i.e. weight loss (Figure 1B), kyphosis and loss of mobility. The presence of a pancreatic tumor was confirmed by macroscopic and histologic examination of the pancreas (Figure 1C). The weight of the different organs of interest was compared in between the control and KIC mice groups (Figure 1D-H), showing a weight gain for the pancreas in which the normal pancreas was almost completely replaced by the tumor, and splenomegaly which is usually observed in inflammatory conditions such as cancer. Conversely, gastrocnemius muscle, liver and gonadal adipose tissue showed decreased weight in KIC mice compared to controls, with an almost complete disappearance of fat tissue. All these features are related to tumor-induced cachexia.

We then analyzed specifically the gastrocnemius muscle by histology on transversal sections (Figure 2), showing decreased overall cross-section area in KIC mice compared to controls (Figure 2A-B). Immunohistology analysis with laminin staining demonstrated muscle cells (fibers) shrinkage shown by decreased fiber diameter (reflecting cross-section area) without modification of the total number of fibers per muscle section (Figure 2C-H), and with a moderate change of the proportion of the different fiber types (Figure S1). Sarcopenia was further evidenced by the accumulation of the Muscle RING-Finger protein-1 (MuRF1) E3 ubiquitin ligase involved in proteolysis driving atrophy, by histology (Figure 2I-J) and Western-blotting (Figure 2K-L). These

data show a pronounced sarcopenia in KIC PDAC mice bearing a PDAC tumor, with a marked loss of gastrocnemius mass associated with decrease in fiber's size and increased proteolysis.

Noninvasive MR investigation shows altered gastrocnemius muscle function

Gastrocnemius muscle function and bioenergetics were investigated longitudinally using noninvasive multimodal magnetic resonance (MR) measurements. We found that muscle volume calculated from MR images was lower in KIC mice bearing a tumor at 9-11 weeks of age, when compared to age-matched controls (21% decrease) as well as to 7-8-week-old (non-tumoral) KIC mice (Figure 3A). This muscle volume loss, which is similar to what was observed *ex vivo* upon necropsy (-28%; Figure 1H), was associated with an almost proportional reduction of the absolute tetanic force which represents the maximal muscle capacity for producing force (-16%; Figure 3B). The specific tetanic force, calculated by scaling the absolute tetanic force to muscle volume, did not differ between KIC and controls at 9-11 weeks of age (Figure 3C), hence indicating that the reduction in absolute tetanic force was fully accounted by muscle loss. In addition, there were no differences among both phenotypes and ages for the twitch force-generating capacity during the 6-min bout of exercise (Figure 3D) and the end-exercise twitch force level (Figure 3E). Overall, these data demonstrate that muscle quality was not altered in KIC mice bearing a tumor. On the other hand, the twitch half-relaxation time averaged over the whole 6-min exercise was longer in KIC mice bearing a tumor when compared to age-matched controls and to 7-8-week-old (non-tumoral) KIC mice (Figure 3F), thereby suggesting that muscle biomechanical properties were disturbed in KIC cancer mice.

We then used dynamic ^{31}P-MR spectroscopy for continuously assessing *in vivo* muscle bioenergetics before (rest), during and after the 6-min bout of exercise. The corresponding changes in PCr and pH over the course of time are shown in Figure 3G and 3H, and quantifications at different time points are shown in Figure 3I to 3N. At rest, there were no differences among phenotypes and ages for PCr level (Figure 3I) and pH (Figure 3J), which indicates that the presence of tumor did not affect the basal bioenergetics status. However, we found that the time constant of post-exercise PCr resynthesis (τPCr) was 43% longer in KIC bearing a tumor compared to age-matched controls (Figure 3K). Given that PCr resynthesis during the postexercise recovery relies

exclusively on oxidative ATP synthesis [25], the longer τPCr reveals that the presence of tumor did alter the mitochondrial function. Accordingly, we found that the maximal oxidative capacity, calculated as the ratio between basal PCr and τPCr [26], was lower in these animals (-31%; Figure 3L). It must be pointed out that the end-exercise PCr level, which reflects the metabolic stress in response to exercise activity, was similar in both phenotypes at 9-11 weeks of age (Figure 3M). These data suggest that the tumor-induced mitochondrial defect would not impair energy supply in exercising muscle, through the compensation of the potent limitation of oxidative ATP production in 9-11-week-old mice by another metabolic pathway. In this sense, we observed that the pH value at the end of the 6-min exercise was lower in KIC mice bearing a tumor compared to age-matched controls (Figure 3N), thus suggesting that the tumor accelerates the glycolytic flux. Collectively, these data show a loss of gastrocnemius strength and lower ATP production by oxidative capacities in KIC PDAC mice, pointing to defective mitochondria in the skeletal muscle of PDAC-bearing mice.

Mitochondrial function and homeostasis are profoundly affected in KIC muscles

Decrease of oxidative activity in cancer KIC muscle shown in Figure 3 was further investigated by Seahorse oxygraphy on isolated mitochondria. Two different assays were implemented to assess coupling activity (Figure 4A) and respiratory complexes activity (Figure 4B). Quantification of mitochondrial parameters showed a decrease in basal respiration, proton leak, and maximal respiration in mitochondria from KIC muscles compared to controls, without noticeable difference in mitochondria-linked ATP production and spare respiratory capacity (Figures 4C to G). The activities of complexes I, II and IV were found to be decreased (Figures 4H to J). Furthermore, abundance of each respiratory complex was measured by Western blotting using a cocktail of oxidative phosphorylation (OXPHOS) antibodies, showing decreased level of the corresponding OXPHOS proteins (Figures 4K-L). A prominent decrease of signal was observed by immunohistofluorescence microscopy using the same OXPHOS antibodies cocktail (Figure 4M). These data show a marked defect in mitochondrial respiratory chain in KIC PDAC muscles.

To further assess the mitochondrial compartment in KIC fibers, we analyzed the mitochondria structure by Transmission Electron Microscopy (TEM) experiments on longitudinal and

transversal sections of the gastrocnemius muscle (Figure 5A). We observed striking modifications of the structure of KIC mitochondria compared to controls, with more elongated and disorganized cristae mitochondria, characterized by higher mean area and diameter (Figures 5B-C and S2A-B) and lower circularity (Figure 5D and S2C). KIC mitochondria seemed to be hyperfused, suggesting defects in mitochondrial dynamics (fusion/fission balance) and quality control by mitophagy. Nonetheless, the number of mitochondria per surface of muscle was found unchanged (Figure 5E). To further address the question of mitochondrial mass, we quantified both the total quantity of mitochondria isolated from whole muscle by protein measurements and the level of mitochondrial DNA (mtDNA) in whole muscle by qPCR. We found a remarkable decrease of mitochondrial proteins and DNA levels in KIC muscles compared to control (Figures 5F and G and S2D-E), which outweighed the decrease in total muscle mass (shown in Figures 1H), suggesting defective mitochondrial homeostasis in sarcopenic muscle. Finally, we monitored some of the main proteins involved in mitochondria homeostasis by Western-blotting (Figure 5H). We observed an increase in Mitofusins and OPA1 involved in mitochondrial fusion, consistently with the hyperfused phenotype. Conversely, we found a decrease in Peroxisome Proliferator-activated Receptor–γ Coactivator 1 alpha (PGC1alpha) involved in mitochondrial biogenenesis and in Transcription Factor A Mitochondrial (TFAM) involved in mitochondrial DNA replication, repair, and transcription. These data show that both the shape and the mass of mitochondria are modified in KIC muscles, demonstrating strong mitochondrial qualitative and quantitative defects in PDAC gastrocnemius muscle.

Molecular pathways involved in mitochondrial homeostasis, metabolism and function are strongly dysregulated in PDAC muscle

To go deeper into the molecular mechanisms underlying mitochondrial defects in PDAC muscles, we performed large-scale transcriptomic and proteomic analyses. Overall, a wealth of information was obtained from these two approaches, such that we try to summarize the major trends below.

Transcriptomic analysis

RNA-sequencing was done on RNA extracted from gastrocnemius muscle. A total of 2304 genes were found to be dysregulated in KIC compared to control muscles, with 1277 upregulated and 1027 downregulated (Figure S3A; up- and down-regulation in blue and red color, respectively). The web-based Ingenuity Pathways Analysis (IPA) shown in Figure 6 pointed to pathways which were expected to be dysregulated, such as autophagy, catabolism of protein, glycolysis and atrophy of muscle with a positive z-score, and skeletal muscle physiology (cell movement of muscle cells, migration of muscle cells, function of skeletal muscle) with a negative z-score. The genes encoding the E3 ubiquitin ligase MuRF1 and MAFBx involved in muscle atrophy (*Trim63* and *FBXO32*, respectively) were found to be highly over-expressed as expected (6- and 5-fold increase, respectively).

We then used the data mining mitoXplorer web-based platform to focus our analysis on mitochondria-associated pathways (Figures 7, S3B-C and S4). A total of 178 genes from the mitoXplorer list of mitochondrial interactome genes were found to be dysregulated in KIC compared to control muscles, with 85 upregulated and 92 downregulated (Figure S3B). IPA of mitochondrial dysregulated pathways (Figure 7) showed three pathways in common with the general IPA: autophagy, glycolysis and atrophy of muscle. In addition, this mitochondrial IPA pointed to nine pathways involved in mitochondria homeostasis and respiratory function, consistently with decreased functional OXPHOS in KIC muscle: depolarization, swelling, and permeabilization of mitochondria with positive z-scores, and respiration, transmembrane potential, quantity, fragmentation and density of mitochondria, and consumption of oxygen with negative z-scores. Interestingly, besides mitochondria homeostasis, mitochondrial IPA pointed to three lipid metabolism pathways (accumulation of lipids, oxidation of lipid, and oxidation of long chain fatty acid), to put in link with the fatty acid metabolism pathway with a positive z-score in the general IPA. The mitoXplorer visual representation of dysregulated genes pointed to amino acid metabolism and OXPHOS as highly dysregulated with multiple up- and down-regulated genes, respectively (Figure S3C and S4). Translation and glycolysis were also among the most dysregulated pathways. Interestingly, metabolic pathways feeding the respiratory chain were found dysregulated: half of the genes involved in the tricarboxylic acid (TCA) cycle were down-regulated, and four lipid metabolism pathways (fatty acid degradation & beta-oxidation, fatty

acid biosynthesis & elongation, fatty acid metabolism, and metabolism of lipids & lipoproteins) were affected. Moreover, this analysis pointed to dysregulations of mitochondrial dynamics and mitophagy genes, in accordance with mitochondria structural alterations observed by TEM.

Notably, the genes encoding Peroxisome proliferator-activated receptor gamma (PPARγ) coactivator-1 (PGC-1) proteins - *Ppargc1a* encoding PGC-1α and *Ppargc1b* encoding PGC-1ß - involved in mitochondrial biogenesis were strongly down-expressed (see the "Transcription (nuclear)" heatmap in Figure S4). Finally, genes involved in reactive oxygen species (ROS) defenses were found to be upregulated including *Nfe2l2* encoding the Nrf2 antioxidant transcription factor (found in the "Replication & Transcription" group Figure S4), which is a mark of oxidative stress.

Proteomic analysis

We also did a proteomic analysis by mass spectrometry of proteins extracted from entire muscle. A total of 154 proteins were found to be dysregulated in KIC compared to control muscles, with 107 upregulated and 47 downregulated (Figure S5A). IPA shown in Figure 8 pointed to dysregulation of muscle physiology pathways (contractility of muscle, muscle contraction, and organization of muscle cells) and multiple metabolic pathways (mostly lipid and protein metabolic pathways, but also nucleotide and DNA metabolism). Thus, dysregulations of muscle physiology and metabolism are common between the general proteomic and transcriptomic analyses.

We then focused our analysis on mitochondria-associated pathways using the mitoXplorer platform (Figures 9, S5B and C and S6). IPA of mitochondrial dysregulated pathways pointed to two pathways (synthesis of reactive oxygen species and oxidative stress) that are connected to two pathways found in the general IPA (metabolism of hydrogen peroxide and quantity of reactive oxygen species), all related to redox metabolism and with positive z-scores (Figures 8 and 9). In addition, the mitochondrial IPA pointed to four pathways, all with negative z-scores, involved in mitochondria energetic and apoptotic functions: consumption of oxygen, concentration of ATP, synthesis of ATP, Apoptosis and cell viability (Figure 9). The mitoXplorer visual representation of dysregulated proteins pointed to OXPHOS, translation, amino acid metabolism and TCA cycle as the major dysregulated pathways (Figure S5C), which is consistent

with the transcriptomic data. Surprisingly, the ROS defense proteins were all found down-regulated at the protein level, when compared with up-regulated ROS defense genes in the transcriptomic data (compare Figure S5C with S3C), which could suggest an altered response to major oxidative stress in KIC muscles.

Common mitochondria-associated pathways between transcriptomic and proteomic analyses

To compare the outcome of transcriptomic and proteomic IPA analyses regarding mitochondrial dysregulated pathways in cachectic cancer muscle, we pointed out the shared (common) pathways in Figure 9. We found 3 common pathways with the same z-score (production/synthesis of reactive oxygen species, glycolysis and metabolism of amino acids) and 4 common pathways with opposite z-score (DNA damage, oxidative stress, consumption of oxygen and autophagy). Figures S7 to 9 show the genes or proteins belonging to each of these 7 common pathways (IPA signatures). The *Dlst* gene, encoding the TCA cycle dihydrolipoyllysine-residue succinyltransferase (Dlst) protein, was the only one to be found in both transcriptomic and proteomic signatures (production/synthesis of reactive oxygen species), and it is down-regulated for both gene expression and protein level. Importantly, it was more meaningful to compare the mitoXplorer signatures shown in Figure S4 and Figure S6 for transcriptomics and proteomics analysis, respectively. We found 16 common genes/proteins, in 4 different groups. Group 1 includes only Sirt2 ("Mitochondrial Signaling" heatmap) which is upregulated in KIC muscle compared to control, both at the level of gene expression and protein. Group 2 includes 7 genes/proteins that are downregulated at both the gene and protein expression levels: Eno3 and Pgam2 ("Glycolysis"), Mrpl19 ("Translation"), Dlst ("Tricarboxylic Acid Cycle"), Pdp1 ("Pyruvate Metabolism"), Dnaja1 ("Protein Stability & Degradation"), and Cyb5b ("Metabolism of Vitamins & Co-Factors"). Group 3 includes 5 genes/proteins that are upregulated at the gene expression level and downregulated at the protein level: Pcca ("Amino Acid Metabolism"), Gpx4 and Gstp1 ("ROS defense"), Aldh7a1 ("Pyruvate Metabolism"), and Aldh1l1 ("Folate & Pterin Metabolism"). Group 4 includes 3 genes/proteins that are downregulated at the gene expression level and upregulated at the protein level: Mrpl45 ("Translation"), Coq3 ("Ubiquinone Biosynthesis"), and Nme1 ("Nucleotide Metabolism"). Collectively, these data point to many

mitochondrial genes and their encoded proteins whose expression and/or stability are dysregulated in cancer cachectic muscle compared to healthy muscle. Several of these genes/proteins are involved in biological processes that are still poorly explored in cancer-associated cachexia, such as nucleotide and folate metabolism, which is of interest in the context of mitochondrial DNA homeostasis.

DISCUSSION

This study provides an in-depth deciphering of mitochondrial dysfunction during PDAC-induced muscle atrophy at the tissular, cellular and molecular level. We confirm that the metabolic organs are considerably affected by the cachexia induced by the pancreatic tumor in the KIC mouse model, with notably the almost complete disappearance of the gonadal adipose tissue. Regarding the gastrocnemius muscle, cachexia is illustrated by the loss of mass (weight and volume) and strength. Muscle mass loss is associated with a diminution in muscle fiber's size, which is a common feature in cancer muscle wasting studies [27]. In contrast, we have not seen any significant changes in the number and type of fibers, in agreement with the fact that not all studies have demonstrated type 1 and 2 fiber differences in cancer muscle wasting studies [27]. The reduction of the size of the fibers is due to decreased protein synthesis and increased proteolysis. The latter involves two processes of protein degradation, the proteasome and autophagy. We evidenced the induction in KIC muscle of the E3 ubiquitin ligase MuRF1 (RNA-seq data, Western-blotting, immunohistology) and MAFBx (RNA-seq data) involved in the proteasomal protein degradation [11]. We also found in the RNA-seq data the induction in KIC muscle of the gene *Sqstm1* gene encoding p62 involved in autophagy, as expected [28].

The detailed analysis of muscle bioenergetics by noninvasive multimodal MR demonstrates lower ATP production by oxidative capacities in KIC PDAC mice that is at least partly compensated by increased glycolysis, which could account for apparently normal muscle activity during exercise. MR data point to dysfunctional mitochondria in the skeletal muscle of PDAC-bearing mice, which was confirmed by oxygraphy analysis. Seahorse (oxygraphy) experiments performed on isolated mitochondria demonstrate a large reduction of mitochondrial respiration in PDAC muscle, resulting from the decrease of the activity (Seahorse data) and abundance (Western-blotting and fluorescence microscopy) of the respiratory complexes.

As the function and the structure of mitochondria are tightly linked [29], we analyzed the gastrocnemius muscle by transmission electron microscopy (TEM). We observed important modifications in the size and shape of mitochondria in PDAC muscle, with the presence of elongated mitochondria (hyperfused-like), without any change in the total number of

mitochondria but with decreased mitochondrial mass. At the molecular level, we looked at proteins involved in mitochondrial fusion (Mitofusins 1 and 2 and OPA1) and fission (DRP1 and FIS1). We found a slight decrease of both Opa1 and Drp1 in KIC muscle at the transcriptomic level (no difference for Mfn1, Mfn2, and Fis1). In contrast, we found the proteins OPA1 and Mitofusin 1 + 2 as up-regulated in KIC muscle by Western-blotting, suggesting that transcriptomic and proteomic modifications of molecules involved in mitochondrial fusion are not related. Regarding mitophagy, the genes Bnip3, Bnip3l, and Pink1 were found down-regulated. One could imagine that mitochondrial hyperfusion in the KIC context is a compensatory mechanism allowing to maintain (rather badly than well...) the functioning of mitochondria in this muscle in full catabolism, and also perhaps to preserve the mitochondria from degradation by autophagy [30]. Finally, the genes encoding PGC-1α and PGC-1ß involved among other roles in mitochondrial biogenesis were strongly down-expressed as expected [28, 31]. Collectively, these data demonstrate a profound alteration of the structure and content of mitochondria in pancreatic cancer muscle, associated with a decrease in mitochondrial respiratory function.

The major originality of this study is the deep deciphering of mitochondrial molecular changes at the transcriptomic and proteomic level. Our data demonstrate large alterations in the metabolism of carbohydrates and proteins in PDAC cachectic muscle as expected. Metabolism of amino acids and glycolysis were among the most dysregulated pathways, consistently with overall altered protein metabolism and loss of OXPHOS function, respectively.

One novel feature highlighted in this study concerns the reactive oxygen species (ROS) metabolism. Also, the inflammatory response is one deregulated pathway shown in Figure 6 that has to be related to the redox alterations [28]. Increased expression of multiple reactive oxygen species (ROS) defense genes suggests oxidative stress prone to affect mitochondrial macromolecules and homeostasis [31]. It should be noted that the proteins involved in antioxidant defense are, on the contrary, downregulated, suggesting a defective production to fight against oxidative stress.

Our data unveil major pathways associated with dysfunctional OXPHOS in PDAC muscle mitochondria, featured by altered function of the mitochondria respiratory complexes, decreased ATP production, and conversely increased production of ROS. These data strongly

support that the main molecular alterations in KIC mitochondria are related to energetic and redox metabolisms.

Other novelties revealed by this study concern the lipid and nucleotide metabolisms. Lipid metabolism pathways were specifically found to be downregulated in KIC muscles and mitochondria, which has to be related to the stringent loss of fat mass in cachectic KIC mice and the physiologically relevant role of fatty acid in mitochondrial respiration via fatty acid oxidation. Interestingly, it was reported that excessive fatty acid oxidation induces muscle atrophy in cancer cachexia [32], suggesting that early deregulation of mitochondrial lipid metabolism could be involved in triggering muscle atrophy in PDAC. In addition, several pathways of DNA metabolism, such as DNA damage, degradation of DNA, nucleotide synthesis, and folate pathway (involved in purines and pyrimidines synthesis) were found deregulated, suggesting a certain level of DNA instability affecting the mitochondrial genome. Interestingly, the decrease of mitochondrial DNA in KIC muscle was even larger that the decrease in mitochondrial mass as measured by protein content, suggesting altered mitochondrial genome homeostasis in PDAC-induced sarcopenia, as has been reported in age-related sarcopenia [33, 34]. In sum, the large amount of data generated by this study provides a wealth of information for the identification of new gene and protein markers of cachexia associated with pancreatic cancer. It would be interesting to further investigate the interactions between mitochondrial DNA alterations and redox and nucleotide metabolism.

A transcriptomic analysis of PDAC cachectic muscle was reported by van der Ende and coll. [15] using the gene expression microarrays data generated by Gilabert et coll on biceps femoris muscle from KIC mice [22]. They highlighted decreased expression of genes involved in mitochondrial fusion, fission, ATP production and mitochondrial density, and increased expression of genes involved in ROS detoxification and mitophagy. We observed these same gene modulations in the same direction in KIC gastrocnemius. In a notable way, we have here largely completed this preliminary study by integrating transcriptomic and proteomic data in cachectic muscle, and by revealing a large number of modulated mitochondrial genes. Importantly, integrating the transcriptome and proteome in KIC muscle showed several common pathways that are deregulated during cachexia, suggesting that considering transcriptome only (for which

diagnostic tools are available in the clinic) would be relevant in further studies.

Importantly, in major pathways, deregulation of genes in one direction (up or down) can be the opposite for the corresponding protein (down or up, respectively). This is consistent with the fact that for one gene, mRNA level (related to gene transcription rate and RNA-stability) is not obligatory correlated with protein level (related to translation rate and protein stability) [35, 36].

The first limitation of this study is the use the KIC PDAC model which is fast (9 weeks) compared to human pathology. Nevertheless, this model is indicative of common molecular pathways involved in cachexia in human and mouse; for example, disruption of mitochondrial morphology and decrease of mtDNA were also observed in the skeletal muscle of cachectic patients [37]. Second, we used only male mice, yet some mechanisms of pancreatic cancer cachexia are sex specific [38]. We postulated that mitochondrial alterations would be similar in males and females, but this question remains to be addressed. Third, this study is lacking molecular data concerning mitochondria in pre-cachectic KIC muscle before the tumor-induced cachexia, that we monitored with noninvasive multimodal magnetic resonance (MR) measurements (7-8-week-old [non-tumoral] KIC mice in Figure 3). It will be very interesting to know whether mitochondrial defects happen before the start of muscle atrophy in PDAC, and initiate sarcopenia as demonstrated in other studies [39-41].

In conclusion, this work demonstrates that muscle atrophy is associated with strong mitochondrial metabolic defects that are not limited to carbohydrates and protein, but concern also lipids, ROS and nucleic acids. Our data provide a frame to guide towards the most relevant molecular markers that would be affected early during tumor development and could be targets in the clinic to limit PDAC-induced cachexia at early stages of the pathology.

METHODS

Genetically-Engineered Mouse Model of Pancreatic Cancer

To assess cancer-induced muscle wasting in a spontaneous tumor model of Pancreatic Ductal Adenocarcinoma (PDAC), LSL-Kras^{G12D};Ink4a/Arf$^{fl/fl}$;Pdx1-Cre (KIC) mice and LSL-Kras^{G12D};Ink4a/Arf$^{fl/fl}$ (KI) control littermates mice were generated in our laboratory. We used only male mice. The genotyping was done by PCR, and mice were screened for the presence of pancreatic tumors at the necropsia at the age of 9-11 weeks. Total body weights were measured weekly from the age of 4 weeks to the sacrifice. At terminal sacrifice, pancreas, liver, spleen, gonadal adipose tissue and both gastrocnemius muscles were harvested and weighted. A piece of each organ and one gastrocnemius muscle were fast frozen in isopentane cooled on dry ice, and stored at −80° C for RNA and protein analysis. One entire gastrocnemius muscle was used to extract mitochondria ex vivo, or fast frozen and stored at −80°C for histological analysis. For pancreas, liver and spleen, a piece was fixed in 4% paraformaldehyde (PFA) and embedded in paraffin for histological and immunohistochemical analysis. All animal care and experimental procedures were performed with the approval of the Animal Ethics Committee of Aix Marseille University under reference #21847-2019083116524081 for mice housed at the CRCM PSEA animal facility or reference #20423-2019042913133817v2 for mice housed at the CRMBM animal facility.

Noninvasive magnetic resonance (MR) investigation of gastrocnemius muscle function

Gastrocnemius muscle function was assessed noninvasively and longitudinally in 5 KIC before (7-8 weeks of age) and after (9-11 weeks) tumor development, and in 7 age-matched control. The gastrocnemius muscle was chosen because it is easily accessible for MR antenna and preferentially activated using our methods [42]. Investigations were performed with a homebuilt cradle designed to be operational inside the 7-Tesla horizontal magnet of a preclinical 70/16 PharmaScan MR scanner (Bruker, Karlsruhe, Germany). This cradle is similar to that described previously [42]. Briefly, it allows (i) to elicit contraction of the left gastrocnemius muscle by transcutaneous electrostimulation, (ii) to measure the resulting contractile force with a

dedicated ergometer composed of a foot pedal coupled to a force transducer, (iii) to perform multimodal MR measurements, and (iv) to maintain prolonged anesthesia by gas inhalation (1.5-2% isoflurane mixed in air) with monitoring of breath rate and regulation of the animal's body temperature at physiological level throughout a feed-back loop. Fourteen consecutive non-contiguous axial slices (1-mm thickness; 0.25-mm spaced) covering the whole left hindlimb were selected. Rapid acquisition relaxation-enhanced (RARE) images of these slices (8 echoes; 5000-ms repetition time; 35-ms TE; 20 x 20 mm^2 field of view; 0.078 x 0.078 mm^2 spatial resolution) were acquired at rest. Muscle function was evaluated throughout a tetanic electrostimulation train (150 Hz; 0.5-s duration) and during a bout of exercise consisting in 6 minutes of repeated isometric contractions electrically induced at a frequency of 1 Hz. Contractile force was recorded and processed using the Powerlab 35 series system driven by the LabChart v8.1 software (AD Instruments, Oxford, United Kingdom). The digital signal was converted to force according to a linear calibration curve and expressed in N. ^{31}P-MR spectra (15 accumulation; 2000-ms repetition time) from the gastrocnemius muscle region were continuously acquired at rest (4-min), during the 6-min exercise bout, and during the following 16-min recovery period. MR data were processed using custom software code written in Python. For each MR image, region of interest was manually outlined so that the corresponding cross-sectional area of the gastrocnemius muscle was measured. Level of phosphocreatine (PCr) and pH were obtained from ^{31}P-MR spectra by a time-domain fitting routine using the AMARES algorithm [43]. The time constant of PCr resynthesis (τPCr) was determined by fitting the PCr time changes during the post-exercise recovery period to a single exponential curve with a least mean-squared algorithm [25]: $\tau PCr = -t/\ln(PCr_t/\Delta PCr)$, where ΔPCr is the extent of PCr depletion measured at the start of the recovery period. The maximal oxidative capacity was calculated as the ratio between the basal PCr level and τPCr [26].

Antibodies and reagents

Total OXPHOS rodent antibodies cocktail was from abcam (mouse, ref ab110413), antibody against Mitofusin1+2 was from abcam (mouse, ref ab57602), antibody against laminin 2α was from abcam (rat, ab11576), antibody against MuRF1 was from abcam (mouse, ab201941),

antibody against β-actin was from Sigma-Aldrich (mouse, A-5316). Antibodies against myosin heavy chain (MHC)-I (mouse, ref M8421), MHC-IIa (mouse, ref SC-71-C) and MHC-IIb (mouse, ref BF-F3-C) were obtained from the Developmental Studies Hybridoma Bank (DSHB), created by the NICHD of the NIH and maintained at The University of Iowa, Department of Biology, Iowa City, IA 52242. The secondary antibody used for Western blotting, Goat anti-mouse IgG conjugated to horseradish-peroxidase (HRP), was from Southern Biotech (Ref 1030-05). The blocking Goat anti-mouse IgG(H+L) was from Jackson laboratories (Ref 115-007-003). Secondary antibodies used for immunofluorescent staining, Goat anti-mouse Alexafluor 350 igG2b (ref A-21140), Goat anti-mouse Alexafluor 488 igG1 (ref A21121), Goat anti-mouse Alexafluor 488 (ref A11029), Goat anti-mouse Alexafluor 594 IgM (ref A-21044), Goat anti-rat Alexafluor 594 (ref A11007) were all from Invitrogen. DAPI reagent was from Thermofisher Scientific (ref 62248).

Hematoxylin, Phloxine and Saffron (HPS) staining

Gastrocnemius muscle cryosections (see below) or microtome sections of deparaffinized and rehydrated pancreas, liver and spleen (5µm-thick) were stained according to a standard protocol. Briefly, the slides were incubated in Mayer's Haematoxilin (Sigma-Aldrich, ref 109249) during 3 min, fast washed in Ethanol 96%-HCl 1% then in water, then submitted to the bluing step during 3 min in sodium bicarbonate buffer (0.1% in water) before to be stained during 30 sec with 2.5% Phloxine solution (Sigma Aldrich, ref P2759), washed and stained 30 sec in Saffron in alcoholic solution (RAL Diagnostics, ref 361500-1000) before final dehydration and mounting. Pictures of the whole slides were acquired with the Axio Imager 2 (ZEISS).

Masson's trichrome staining

Gastrocnemius muscle cryosections were stained using Trichrome stain kit from abcam (ref ab150686) according to manufacturer's instructions. Briefly, sections were incubated in Bouin's fluid for 60 min followed by a 10 min cooling period then washed in water until they were completely clear before to be stained for 5 min in Weigert's Iron Hematoxylin. After water washing, Biebrich Scarlet / Acid Fuchsin solution was applied to slides for 15 min followed by another water wash. Differentiation was made in Phosphomolybdic/Phosphotungstic Acid

solution for 15 min followed by incubation in Aniline Blue solution for 10 min without rinsing. Then slides were washed in water and incubated in 1% Acetic Acid solution for 5 min before final dehydration and mounting of the sections. Pictures of the whole slides were acquired with the Axio Imager 2 (ZEISS).

Immunofluorescence

Cross sections of frozen gastrocnemius muscle (10 µm) were done at -22°C on a cryostat and collected on Superfrost plus glass slides. Cryosections were then processed for staining. In detail, sections were dried at 37°C for 10 min, fixed in 4% PFA for 10 min before being permeabilized in phosphate-buffered saline (PBS)1X+Triton 0.2% (PBS-T) for 30 min. Sections were blocked and saturated with PBS-T+2% BSA+2% Goat Serum for 1 hour, washed 3 times in PBS1X for 5 min, blocked with Goat anti-mouse IgG(H+L) (1:1000) for 1h if necessary, washed 3 times in PBS1X for 5 min before to be incubated with primary antibody for 2h at room temperature (RT). After 3 washes in PBS1X for 5 min, sections were incubated with adapted secondary antibodies for 1h at RT, washed in PBS, and incubated with DAPI for nuclear staining before final wash and mounting with Prolong fold antifade mounting medium from Thermofisher Scientific (ref P36934). Pictures of the whole slides were acquired with the Axio Imager 2 (ZEISS), and the cross-sectional area, fiber Feret's diameter (longest distance (µm) between any two points within a given fiber), and MuRF1 positive stained area in muscle sections were measured automatically by ImageJ software. The following primary antibodies dilutions were used: Total OXPHOS rodent antibodies cocktail (1:200), anti-Laminin 2α (1:200), anti-MuRF1 (1:200), anti-MHC-I (1:500), anti-MHC-IIa (1:600), anti-MHC-IIb (1:1000). Adapted Alexafluor-conjugated secondary antibodies were used at 1:500 dilutions.

Transmission Electron Microscopy

Mice were transcardially perfused with cold PBS (10 mM, pH7.4), followed by 2% glutaraldehyde solution in 0.1 M cacodylate buffer (pH 7.4), under ketamine (150 mg/kg) and xylazine (20 mg/kg) anesthesia. After necropsia, gastrocnemius muscle samples were immediately fixed in a 2% glutaraldehyde solution in 0.1 M cacodylate buffer (pH 7.4), postfixed in 1% osmium tetroxide in

0.1 M cacodylate buffer, dehydrated in increasing concentration of ethanol followed by acetone and embedded in Epon. One µm thick sections were stained with toluidine blue to verify the orientation of the muscle tissue prior the ultrathin sectioning. Ultrathin sections were cut in longitudinal or transverse orientation using an Ultracut UC7 ultramicrotome (Leica) and mounted on Coper carbon-formvar coated grids. Uranyl acetate and lead citrate-stained sections were imaged using a FEI G2 electron microscope (FEI) with 200 KeV. Digital micrographs were captured using a Veleta (Olympus) digital camera. Individual mitochondria from CTRL (n=3) and KIC (n=3) mice were manually traced in longitudinal and transverse orientations using ImageJ (NIH), to quantify the following morphological and shape descriptors: area (in μm^2), circularity ($4\pi\cdot$(surface area/perimeter^2)), and Feret's diameter (longest distance (µm) between any two points within a given mitochondrion).

Protein isolation and Western blot analysis

Gastrocnemius muscle samples were lysed in lysis buffer (10% N-Deoxycholate, 0.1% SDS, 1% Triton X-100, 10 mM Tris pH 8, 140 mM NaCl, phosphatases/proteases inhibitors (Sigma-Aldrich), 1% phenylmethylsulfonyl fluoride, 1 mM sodium fluoride (NaF), 100 µM sodium orthovadanate (Na3VO4), 40 mM beta glycerophosphate) in beads tubes from Precellys lysing kit for hard tissue (ref P000917-LYSK0-A, 3x Cycle 1500 rpm, 15 sec of mix, 10 sec of rest) and incubated at 4°C for 30 min to solubilize proteins before centrifugation (10.000g, 10 min, 4°C). Supernatants were collected and protein concentration evaluated using BioRad Protein assay. Proteins were diluted in 1X Laemmli sample buffer and heated at 95°C for 10 min in the presence of β-mercaptoethanol (Sigma) (except for OXPHOS cocktail antibody according to manufacturer's instructions). Whole protein extracts (25-75 µg per lane) were resolved by SDS–polyacrylamide gel electrophoresis (SDS–PAGE) using a 10% (vol/vol) acrylamide gel and transferred onto 0.2 µm nitrocellulose membranes (GE Healthcare). After a blocking step (5% (wt/vol) non-fat milk in TBS O/N at 4°C), membranes were incubated with primary antibodies diluted in 5% (wt/vol) non-fat milk in TBS 0.1% Tween O/N at 4 °C. Following dilutions of primary antibodies were used: anti-OXPHOS cocktail (1:500), anti-MuRF1 (1:200), anti-β-actin (1:10,000). After three washes in TBS 0.1% Tween, membranes were incubated 2h at RT with HRP-conjugated secondary antibodies at

1:5000 in 5% (wt/vol) non-fat milk, 5% in TBS 0.1% Tween. ECL protein detection (Millipore) was performed with a Fusion Fx7 chemiluminescent imager and the quantifications of the amounts of proteins of interest were determined by densitometry using ImageJ software (NIH) and normalized to actin or to total proteins stained with Ponceau Red.

Mitochondrial Isolation

Mitochondria were extracted directly ex vivo from entire gastrocnemius muscle samples. Briefly muscles were collected, cut in petri dishes and incubated in 5 mL of Isolation Mitochondrial Buffer 1(IBM1) (BSA 0.2%, EDTA 10mM, KCL 50mM, Tris/HCl 50mM, Sucrose 67mM, pH 7,4) with 0.05% trypsine for 1h under agitation at 4°C. After a brief centrifugation (3 min, 200g, 4°C), supernatant was removed and muscle pieces collected and homogenized in IBM1 using Teflon glass pestle homogenizer in ice. Mitochondria were isolated via differential centrifugation. Briefly, the homogenate was centrifuged (10 min, 1200g, 4°C) and the supernatant decanted into a new tube. This fraction was centrifuged again (10 min, 8000g, 4°C) to obtain a mitochondrial pellet. Supernatant which contains soluble proteins was carefully removed and the mitochondrial pellet was washed and resuspended carefully in 200 µL of Isolation Mitochondrial Buffer 2 (IBM2) (D-Mannitol 200mM, EGTA 5mM, Tris/HCl 10mM, Sucrose 70mM, pH 7,4) and diluted in 6 mL of IBM2 followed by a centrifugation to purify mitochondria. This step was repeated a second time before resuspension of mitochondrial pellet in 50-100 µL of IBM2 at 4°C. BCA assay was performed with a spectrophotometer to evaluate mitochondria protein concentrations before oxygraphic measurements.

Mitochondrial oxygraphic respiration assay

Seahorse XF24 instrument (Agilent Technologies) was equilibrated at 37 °C and XF Sensor cartridge hydrated overnight. Mitochondria isolated from gastrocnemius muscle (1 µg equivalent proteins) were diluted in 50 µL final volume of 1x Mitochondrial Assay Solution (MAS) (D-Mannitol 200mM, EGTA 5mM, Tris/HCl 10mM, Sucrose 70mM, pH 7,4), and plated in each well of the XF24 plate after supplementation with ADP (5mM), succinate (10mM) and rotenone (2µM) for the coupling assay, or pyruvate (5mM), malate (1mM) and FCCP (4µM) for the electron flow

experiment. The XF24 plate containing mitochondria with substrates was centrifuged (20 min, 2000g, RT) with microplate adaptor. After centrifugation, 450 µl of 1× MAS containing suitable substrates was added to each well, and the plate was incubated in a non-CO2 incubator at 37°C for 8–10 min. The XF cartridge was prepared for injections for ports A, B, C and D during plate centrifugation. Stock solutions of oligomycin, FCCP, rotenone and antimycin A were made in DMSO. The injections for coupling experiment were prepared as follows: 55 µl of oligomycin (40µM in 1× MAS containing suitable substrates), 60 µL of FCCP (40µM), and 65 µL of Antimycin A (80µM) were loaded into ports A, B and C, respectively. The final concentrations in wells were 4 µM oligomycin, 4 mM FCCP and 8 µM antimycin A. The injections for electron flow experiment were prepared as follows: Port A, 20µM rotenone (55 µl in 1× MAS containing suitable substrates), Port B, 50 mM succinate (60 µl), Port C, 80µM antimycin A (65 µl), and port D, 100 mM ascorbate with 1 mM TMPD (70 µl). The final concentrations were 2 µM rotenone, 5 mM succinate, 8 µM antimycin A and 10 mM ascorbate with 100 µM TMPD. The cartridge was calibrated by the Seahorse XF24 machine, then the XF plate containing mitochondria was introduced into the machine and the assay continued using a protocol of 1 min of Mixing, 20 sec of Waiting, 2 min of measurement cycles done 2 times after calibration and after each injection.

Total DNA isolation from gastrocnemius skeletal muscle

Total DNA (genomic and mtDNA) was isolated from ≈20-30 mg of gastrocnemius skeletal muscle. Briefly, tissues were lysed overnight at 50°C under agitation in DNA lysis buffer (0.2% SDS, 100 mM Tris pH8, 200mM NaCl, 500nM EDTA) with 200 µg/mL Proteinase K RNA grade (Invitrogen, ref 25 530-049) followed by RNAse incubation (ThermoFisher, ref AM2294) to remove RNA contamination. Samples were centrifuged (12.000g, 10 min, RT) and the supernatant was transferred and mixed in equal volume of absolute ethanol to allow DNA precipitation. Samples were centrifuged (12.000g, 10 min, RT), supernatant was removed and DNA pellet resuspended in RNAse/DNAse free water. DNA concentration and purity were assessed using spectrophotometer.

mtDNA copy number analysis

Mitochondrial DNA copy number, relative to the diploid chromosomal DNA content, was quantitatively analyzed from gastrocnemius muscle total DNA using MxPro Mx3000P real-time PCR Analyzer (Agilent technologies / Stratagene). Primers were designed around mt12S and mtCOX-III regions of the mitochondrial genome. NDUFV1 (NADH:Ubiquinone Oxidoreductase Core Subunit V1) gene was used as nuclear housekeeping gene.

Transcriptomic analysis by bulk RNA sequencing

Total RNA Isolation from gastrocnemius skeletal muscle

Total RNA was isolated from ≈25mg of the gastrocnemius skeletal muscle using both TRIzol (Invitrogen) and the Qiagen total RNA isolation kit (Qiagen, ref 74004) to avoid protein and extracellular matrix accumulation in the columns. Briefly, muscle piece was lysed in 600 µL RLT Buffer (from Qiagen kit) with 1% β-Mercaptoethanol using beads tube from Precellys lysing kit for hard tissue (ref P000917-LYSK0-A, 3x Cycle 1500 rpm, 15 sec of mix, 10 sec of rest) and directly centrifuged 3 min at 10.000g at RT. Supernatant was transferred in 400µL of TRIzol and incubated for 5 min at RT followed by addition of 150µL of Chloroforme. Tubes were carefully mixed and incubated 3 min at RT before centrifugation (12.000g, 5min, 4°C). The transparent upper phase containing RNAs was transferred in a tube containing 500 µL of 70% Ethanol, mixed and transferred inside Qiagen RNA isolation kit columns according to manufacturer's instructions followed until the end of extraction. DNA samples were treated with RNase-free DNase on Qiagen spin-columns to remove DNA contamination. RNA integrity and concentration were assessed using the Agilent 2100 Bioanalyzer (Agilent Technologies, Palo Alto, CA). The average RIN (RNA integrity number) values for all samples was comprised between 9.3 and 10, ensuring a high quality of isolated RNAs.

Bulk RNA sequencing

The preparation of mRNA libraries was realized following manufacturer's recommendations (kapa mRNA HyperPrep from ROCHE). Final samples pooled library prep were sequenced on ILLUMINA Novaseq 6000 with S1-200cycles cartridge (2x1600Millions of 100 bases reads), corresponding to 2x30Millions of reads per sample after demultiplexing.

Bulk RNA sequencing data analysis

Quality control has been performed on the fastq files using FastQC (v0.11.9) (http://www.bioinformatics.babraham.ac.uk/projects/fastqc). To map the sequenced reads to the mouse reference genome (GRCm39 from NCBI), we made use of STAR (v2.7.3a) [44]. From these mapped reads, gene counts were then quantified using featureCounts (v2.0.1) [44]. Starting from the raw gene counts, normalization and differential expression analysis have then been performed using DESeq2 (v 1.22.2) [44]. Resulting from the differential expression analysis, genes were defined as significantly deregulated when the false discovery rate, related to the fold change, was lower than 0.05.

Proteomic analysis by mass spectrometry

Sample preparation and mass spectrometry

Proteomes from gastrocnemius muscles prepared from control and KIC mice were compared by label free quantitative mass spectrometry analysis. Briefly, 15µg of each lysate prepared from muscle was loaded on NuPAGE 4-12% Bis-Tris acrylamide gels (Life Technologies) and run at 80V for 8 min to stack proteins in a single band. Bands were cut from the gels following Imperial Blue staining (Thermo Fisher Scientific) and were submitted to a classical in-gel trypsin digestion after protein reduction and cysteine alkylation with iodoacetamide [45]. Peptides were extracted from the gel and dried under vacuum. Each sample was reconstituted with 0.1% trifluoroacetic acid in 2% acetonitrile and analysed thrice by liquid chromatography (LC)-tandem mass spectrometry (MS/MS) using an Orbitrap Fusion Lumos Tribrid Mass Spectrometer (ThermoFisher Scientific, San Jose, CA) online with a nanoRSLC Ultimate 3000 chromatography system (ThermoFisher Scientific, Sunnyvale, CA). For each run, peptides were first concentrated on a pre-column (C18 PepMap100, 2 cm × 100 µm I.D, 100 Å pore size, 5 µm particle size) and washed in water containing 0.1% trifluoracetic acid. In a second step, peptides were separated on a reverse phase LC EASY-Spray C18 column (PepMap RSLC C18, 50 cm × 75 µm I.D, 100 Å pore size, 2 µm particle size) at 300 nL/min flow rate with following parameters: After column equilibration using 3% of solvent B (20% water - 80% acetonitrile - 0.1% formic acid), peptides were eluted from the analytical column by a two steps linear gradient (2.4-22% acetonitrile/H2O; 0.1% formic acid for 130 min and 22-32% acetonitrile/H2O; 0.1 % formic acid for 15 min). MS analysis was performed

following peptide ionization in the EASY-Spray Nano-source in front of the Orbitrap Fusion Lumos Tribrid under a spray voltage set at 2.2 kV and the capillary temperature at 275 °C. The Orbitrap Lumos was used in data dependent mode to switch consistently between MS and MS/MS. Time between Masters Scans was set to 3 seconds. MS spectra were acquired with the Orbitrap in the range of m/z 400-1600 at a FWHM resolution of 120 000 measured at 400 m/z. AGC target was set at 4.0e5 with a 50 ms Maximum Injection Time. For internal mass calibration the 445.120025 ion was used as lock mass. The more abundant precursor ions were selected and collision-induced dissociation fragmentation was performed in the ion trap to have maximum sensitivity and yield a maximum amount of MS/MS data. Number of precursor ions was automatically defined along run in 3s windows using the "Inject Ions for All Available parallelizable time option" with a maximum injection time of 300 ms. The signal threshold for an MS/MS event was set to 5000 counts. Charge state screening was enabled to exclude precursors with 0 and 1 charge states. Dynamic exclusion was enabled with a repeat count of 1 and duration of 60 s.

Data Processing Protocol

Relative intensity-based label-free quantification (LFQ) was processed using the MaxLFQ algorithm from the freely available MaxQuant computational proteomics platform, version 1.6.3.4 [46, 47]. The acquired raw LC Orbitrap MS data were first processed using the integrated Andromeda search engine [48]. Spectra were searched against the Mus Musculus proteome extracted from UniProt on December 2020 and containing 55508 entries (UP000000589). The false discovery rate (FDR) at the peptide and protein levels were set to 1% and determined by searching a reverse database. For protein grouping, all proteins that cannot be distinguished based on their identified peptides were assembled into a single entry according to the MaxQuant rules. The statistical analysis was done with Perseus program (version 1.6.14.0) from the MaxQuant environment (www.maxquant.org). Quantifiable proteins were defined as those detected in above 70% of samples in one condition or more. Protein LFQ normalized intensities were base 2 logarithmized to obtain a normal distribution. Missing values were replaced using data imputation by randomly selecting from a normal distribution centered on the lower edge of the intensity values that simulates signals of low abundant proteins using default parameters (a downshift of 1.8 standard deviation and a width of 0.3 of the original distribution). To determine

whether a given detected protein was specifically differential, a two-sample t-test was done using permutation-based FDR-controlled at 0.05 and employing 250 permutations. The p value was adjusted using a scaling factor s0 with a value of 1 [49]. From the results of the statistical analysis proteins with false discovery rate, related to the fold change, lower than 0.05 were then defined as dysregulated. This analysis included 4 biological replicates of control mice and 5 KIC mice. Each biological replicate was injected twice on the instruments.

Enrichment analysis

Enrichment analysis was performed both on the differentially expressed genes and proteins through the use of IPA (QIAGEN Inc., bioinformatics.com/products/ingenuity-variant-analysis). Differentially expressed genes and proteins data have also been uploaded on the MitoXplorer web platform to explore mitochondrial dynamics in the different conditions [51]. Heatmaps were generated on MitoXplorer web platform.

Data availability

Gene expression data were deposited in the Gene Expression Omnibus repository at NCBI (#XXX). The mass spectrometry proteomics data, including search results, have been deposited to the ProteomeXchange Consortium (www.proteomexchange.org) [52] via the PRIDE [53] partner repository with the dataset identifier PXD036752.

Statistical analysis

We used a Mann-Whitney non-parametric test to compare two experimental groups. One way or two-way ANOVA, followed by the appropriated multiple comparison test, was used when comparing more than two experimental groups. In all figures, data are presented as mean ± standard error of the mean (SEM) and exact n values used to calculate the statistics are indicated. All statistical analyses were performed using GraphPad Prism 8 (GraphPad Software). P-values < 0.05 were considered statistically significant.

FIGURE LEGENDS

Figure 1. Spontaneous PDAC KIC mouse model show an obvious cachexia phenotype with adipose tissue and muscle loss associated with cancer.

(A) Schematic representation of the overall study. **(B)** Total body weight analysis during disease progression (from 4 to 11 weeks of age) in KIC and CTRL male mice. Data are mean +/- 95% of CI and n represents the total number of mice analyzed in each group. Two-way ANOVA Bonferroni test; n=15 or more for control and KIC mice per time-point; **p<0.01, ****p<0.0001. **(C)** Representative HPS staining of pancreas from healthy control versus cancer KIC mice. Dark arrows point to stromal fibrotic areas relative to pancreatic ductal adenocarcinoma. Scale bar = 500 µm. **(D-H)** Total tissue weights of (D) Pancreas, (E) Liver, (F) Spleen, (G) Gonadal adipose tissue and (H) Gastrocnemius muscle of healthy control mice versus end-stage (9-11 weeks) cancer KIC mice. n=17 control and n=16 KIC. Data are mean +/- SD. For the gastrocnemius muscle, the weight mean of the two muscles of each individual was used to calculate the mean. Unpaired two-tailed Mann Whitney t-tests; *p<0.05, **** p<0.0001, and n represents the number of mice that were analyzed.

Figure 2. PDAC mice show muscle atrophy associated with fiber's size decrease and activation of the proteasome pathway.

(A) Representative images of transversal sections of gastrocnemius muscle from healthy control and cancer KIC male mice following Masson's trichrome staining. Scale bars, 1mm. **(B)** Diagrams of cross section areas of gastrocnemius muscle from healthy control mice and cancer KIC mice (n=8/group). Data are mean +/- SD. Unpaired two-tailed Mann Whitney t-tests; **p<0.01, and n represents the number of mice that were analyzed. **(C)** Representative immunostaining of gastrocnemius muscle cross sections from control and KIC mice stained with DAPI (blue; nuclei), and an anti-laminin antibody (red) to evaluate muscle fiber's size. Scale bars, 40µm. **(D-E)** Number of muscle fibers counted in gastrocnemius cross sections from control and KIC mice (D), and mean fiber's (100) minimal Feret's diameter in gastrocnemius muscle from control and KIC mice (E). Data are mean +/- SD. Unpaired two-tailed Mann Whitney t-tests; ns = non-significant,

****p<0.0001, and n represents the number of mice that were analyzed. **(F-H)** Muscle fiber's size distribution in gastrocnemius muscle from control and KIC mice. Minimal Feret's diameters were determined in gastrocnemius cross-sections from immunofluorescent staining above. Hundred fiber diameters were counted per group. The values are expressed as the percentage of the total quantified fibers from 10 to 160µm, and the image counts are representative of n=5 mice muscle cross sections used for each experimental condition. Values correspond to the mean ± SEM. The line represents the median distribution of minimal Feret diameters observed in healthy control versus cancer KIC mice (F)**,** and the mean percentage of muscle fiber's distribution is represented for the Healthy CTRL group (G) and Cancer KIC group (H). **(I)** Representative immunostaining of transverse sections of gastrocnemius muscle from control and KIC male mice stained for MuRF1 (green) to evaluate muscle atrophy, laminin (red) to evaluate muscle fibers, and merged images. Scale bars, 40µm. **(J)** MuRF1 immunofluorescent staining quantification in transversal sections of gastrocnemius muscle from control and KIC mice. Data are mean +/- SEM. Unpaired one-tailed Mann Whitney t-tests; **p<0.01 and n represents the number of mice that were analyzed. **(K)** Representative immunoblot for MuRF1 in gastrocnemius muscle from CTRL and KIC mice (n=5/group). **(L)** Quantification of immunoblots to show the MuRF1 protein levels in gastrocnemius muscle from CTRL and KIC mice. The relative protein amount was calculated from the control mean in two different experiments. n=5 mice/group. Data are mean +/- SD. Unpaired two-tailed Mann Whitney t-tests; **p<0.01 and n represents the number of mice that were analyzed.

Figure 3. Noninvasive MR investigation of gastrocnemius muscle function and bioenergetics.
(A) Gastrocnemius muscle volume was calculated from MR images. Absolute **(B)** and specific **(C)** force production in response to a tetanic electrostimulation train (150 Hz; 0.5-s duration). **(D)** Twitch force-generating capacity (expressed as percent of maximal twitch force value) during the 6-min bout of exercise performed simultaneously to the dynamic ^{31}P-MRS acquisition. **(E)** Twitch force level at the end of the 6-min bout. **(F)** Twitch half-relaxation time averaged over the whole bout of exercise. Changes in PCr level **(G)** and pH **(H)** throughout the 6-min exercise and the 16-min post-exercise recovery period; for both panels, the first time-point (t = 0) indicates the basal

value. PCr level **(I)** and pH **(J)** measured in resting muscle. Time constant of PCr resynthesis **(K)** and maximal oxidative capacity **(L)**. The drop of PCr **(M)** and acidosis **(N)** were determined at the end of the 6-min bout of exercise. Data are means ± SEM. Controls, n = 7; KIC, n = 5. All samples were normally distributed according to the Shapiro-Wilk test. Significant differences were determined by two-factor (group × age) repeated measures ANOVA followed when appropriate by Tukey-Kramer post-hoc multiple comparison tests. *p<0.05, **p<0.01, ***p<0.001.

Figure 4. Cancer-associated sarcopenia is correlated with a decrease of mitochondrial respiratory activity and respiratory complexes.

(A-B) Representative Seahorse XF oxygen consumption rate assays performed on mitochondria isolated from gastrocnemius muscle of healthy control and cancer KIC mice. The curves were normalized to 1 µg of mitochondrial protein (the assays were done with 2.5 µg of mitochondria). **(A)** Mitochondrial coupling assay. The analysis medium was supplemented with ADP (5mM), succinate (10mM), and rotenone (2µM). **(B)** Electron transport chain assay performed on the same samples of isolated mitochondria. The analysis medium was supplemented with pyruvate (5mM), malate (1mM) and FCCP (4µM) to allow maximal respiration. Data are mean +/- SD and n represents the number of mice analyzed. Two-way ANOVA Bonferroni test; ns = non-significant, *p<0.05, *** p<0.001, **** p<0.0001. **(C-J)** Quantification of the different parameters of mitochondrial respiratory activity, normalized per µg of mitochondrial protein. **(C-G)** Parameters calculated from the mitochondrial coupling assay. **(C)** Basal respiration, measured as the basal OCR subtracted from the background OCR (i.e. OCR after antimycin A addition). **(D)** Proton leak, measured as the OCR after oligomycin addition subtracted from the background OCR. **(E)** ATP production from mitochondria, measured as the basal OCR subtracted from the OCR after oligomycin addition. **(F)** Maximal respiration, measured as the OCR after FCCP addition subtracted from the background OCR. **(G)** The spare capacity is the difference between maximal and basal mitochondrial respiration. **(H-J)** Respiratory complexes activities calculated from the OCR values obtained in the Electron transport chain assay. **(H)** Complex I activity, measured as the basal OCR subtracted from the OCR after rotenone addition. **(I)** Complex II activity, measured as the difference between succinate-driven OCR and OCR after antimycin A addition. **(J)** Complex

IV respiration, measured as the difference between TMPD-driven OCR and OCR after antimycin A addition. Data are mean +/- SD. Unpaired two-tailed Mann Whitney t-tests; ns = non-significant, *** p<0.001, ****p<0.0001; n represents the number of mice analyzed per condition. **(K)** Representative immunoblot for mitochondrial complexes using the rodent cocktail OXPHOS antibodies specific of one protein for each complex: CI (NFUDB8), CII (SDHB), CIII(UQCRC2), CIV(MTCO1), CV(ATP5A), in gastrocnemius muscle from CTRL and KIC mice (n=5/group). **(L)** Relative protein amount of CI (NFUDB8), CII (SDHB), CIII(UQCRC2), CIV(MTCO1), CV(ATP5A) in gastrocnemius muscle from CTRL and KIC male mice. The relative protein amount was calculated from the mean of CTRL from 2 different experiments. n=5 mice/group. Data are mean +/- SD. Unpaired two-tailed Mann Whitney t-tests; ns = non-significant with p-value indicated above, *p<0.05, **p<0.01. **(M)** Representative immunostaining of gastrocnemius muscle cross sections from control and KIC mice stained for mitochondrial electron transport chain complexes I to V (green) to evaluate mitochondrial mass, DAPI (blue) to evaluate nucleus, laminin (red) to evaluate muscle fibers, and merged images as indicated. Scale bars, 100µm.

Figure 5. Mitochondrial structure is profoundly altered in KIC muscles

(A-D) Transmission electron microscopy (TEM) analysis of muscles showing altered mitochondria in cancer mouse muscle. **(A)** Representative TEM micrographs of longitudinal and transversal sections of gastrocnemius muscles from CTRL and cancer KIC mice showing mitochondria ultrastructure. Scale bar = 1µm or 0.2 µm. Yellow triangles point to mitochondria. **(B-D)** Quantification of mitochondria morphological characteristics: **(B)** mitochondrial area (µm²), **(C)** mitochondrial minimal Feret's diameter, and **(D)** mitochondrial circularity in longitudinal sections of gastrocnemius muscles from CTRL healthy mice and cancer KIC mice. n=3 mice/group and 100 mitochondria measured/mouse. Data are mean +/- SD. Unpaired two-tailed Mann Whitney t-test. **** p<0.0001. **(E)** Quantification of the number of mitochondria per mm² in longitudinal and transversal sections of gastrocnemius muscles from CTRL healthy mice and Cancer KIC mice. n=3 mice/group and 15 or more pictures have been taken and measured/mouse. Data are mean +/- SD. Unpaired two-tailed Mann Whitney t-test; ns = non-significant. **(F)** Mitochondrial mass of total isolated mitochondria (in µg of proteins), normalized by the related entire gastrocnemius

muscle mass (in mg) in CTRL and KIC mice. Data are mean +/- SD; n=6 mice/group. Unpaired two-tailed Mann Whitney t-tests; **p<0.01. **(G)** Relative mitochondrial DNA content in gastrocnemius muscle of CTRL and KIC mice using relative level of mtCOX3 (left) and mt12S (right) as mitochondrial genes normalized on gNDUFV1 as nuclear gene. Data are mean +/- SD, n=8 mice/group. Unpaired two-tailed Mann Whitney t-tests, ****p<0.0001. **(H)** Representative immunoblots for Mitofusin1+2 and OPA1 (involved in mitochondrial fusion), PGC-1α (involved in mitochondrial biogenesis), TFAM (involved in mitochondrial DNA replication, repair and transcription) and Actin as loading control in gastrocnemius muscle from CTRL (n=5) and KIC (n=4) mice.

Figure 6. Transcriptomic analysis of total dysregulated genes in cancer sarcopenic muscles.
Ingenuity Pathways Analysis (IPA) showing functions, pathways and diseases significantly dysregulated in gastrocnemius muscle of cancer KIC mice compared to healthy control mice, associated with all genes with significant dysregulation (FDR>0.05) = 2304 genes. Each process is represented using z-score>0.5 as upregulated (blue) or downregulated (red), and the significance represented as -log(p-value) with black dots connected with a dotted line.

Figure 7. Transcriptomic analysis demonstrates multiple mitochondria-associated gene dysregulations in cancer sarcopenic muscles.
Ingenuity Pathways Analysis (IPA) showing functions, pathways and diseases significantly dysregulated in gastrocnemius muscle of cancer KIC mice compared to healthy control mice, associated with genes of the mitochondrial interactome extracted from MitoXplorer tool with significant dysregulations (FDR>0.05) = 178 genes. Each process is represented using z-score>0.5 as upregulated (blue) or downregulated (red), and the significance represented as -log(p-value) with black dots connected with a dotted line.

Figure 8. Proteomic analysis showing total proteins dysregulated in cancer sarcopenic muscle.
IPA enrichment analysis of dysregulated functions, pathways and diseases in gastrocnemius muscle of cancer KIC compared to control mice, associated with all proteins with significant

dysregulations (p-value<0.05) = 360 proteins. Each process is represented using z-score>0.5 as upregulated (blue) or downregulated (red), and the significance represented as –log(p-value) with black dots connected with a dotted line.

Figure 9. Proteomic analysis shows that numerous mitochondrial proteins are dysregulated in cancer sarcopenic muscle.

IPA enrichment analysis of dysregulated functions, pathways and diseases in gastrocnemius muscle of cancer KIC compared to control mice, associated with proteins of the mitochondrial interactome extracted from MitoXplorer tool with significant dysregulations; (p-value<0.05, peptide>1, log2(Foldchange)>0.5) = 53 proteins. Each process is represented using z-score>0.5 as upregulated (blue) or downregulated (red), and the significance represented as –log(p-value) with black dots connected with a dotted line.

LEGEND SUPPLEMENTAL FIGURES

Figure S1. The proportion of the different fiber types is moderately modified in PDAC atrophic muscle (related to Figure 2).

(A) Representative immunostaining of transversal sections of gastrocnemius muscle from healthy control and cancer KIC male mice stained for MHC-IIb (red), MHC-IIa (green), and MHC-I (blue). Scale bars, 40µm. **(B)** MHC-fiber-type distribution mean in gastrocnemius muscles from CTRL and KIC mice (n=5 mice/group). **(C)** MHC-fiber-type distribution in gastrocnemius muscle from control and KIC mice (n=5 mice/group). Data are mean +/- SEM. Unpaired two-tailed Mann Whitney t-tests; ns = non-significant, **p<0.01. The scheme under the graph illustrates the different fiber type characteristics.

Figure S2. Mitochondrial morphology is profoundly altered in KIC muscles (related to Figure 5).

(A-C) Distribution of mitochondria morphological characteristics in percentage (%) of **(A)** mitochondrial area (µm²), **(B)** mitochondrial minimal Feret's diameter, and **(C)** mitochondrial circularity in longitudinal sections of gastrocnemius muscles from CTRL and cancer KIC mice. n=3 mice/group and 100 mitochondria measured/mouse. **(D)** Muscle weight of entire gastrocnemius muscle used for mitochondria isolation and normalized mitochondrial mass quantification shown in Figure 5F. Data are mean +/- SD; n=6 mice/group. Unpaired two-tailed Mann Whitney t-tests; **p<0.01. **(E)** Total mass (in protein equivalent) of mitochondria isolated from entire gastrocnemius muscle from CTRL and KIC mice. Data are mean +/- SD; n=6 mice/group. Unpaired two-tailed Mann Whitney t-tests; **p<0.01.

Figure S3. Transcriptomic analysis of cancer sarcopenic muscles demonstrates obvious mitochondria-associated gene dysregulation (related to Figures 6 and 7)

(A) Heatmap representing total number of dysregulated genes (FDR<0.05) in gastrocnemius muscle from cancer KIC mice (n=4) compared to healthy CTRL mice (n=4). **(B)** Heatmap representing dysregulated genes from mitochondrial interactome after MitoXplorer selection (FDR<0.05) in gastrocnemius muscle from the same mice as (A). **(C)** Mitochondrial interactome of down- or up-dysregulated genes involved in mitochondrial processes in KIC gastrocnemius muscle compared to CTRL (muscle RNA n=4 for each condition). Genes have been selected from total dysregulated genes with FDR<0.05, and affiliated to processes after enrichment using MitoXplorer tool.

Figure S4. Cancer sarcopenic muscles demonstrate obvious mitochondria-associated genes dysregulation (related to Figure S3C).

Heatmaps showing log2 (Fold change) of differentially dysregulated genes involved in mitochondrial processes (based on FDR<0.05) in cancer KIC gastrocnemius muscle compared to healthy CTRL (muscle RNA n=4 for each condition).

Figure S5. Proteomic analysis on Cancer sarcopenic muscles demonstrate obvious mitochondrial associated gene dysregulation (related to Figure 8 and 9).

(A) Heatmap representing total number of dysregulated proteins in gastrocnemius muscle from cancer KIC mice (n=5) compared to healthy CTRL mice (n=4). **(B)** Heatmap representing dysregulated proteins from mitochondrial interactome after MitoXplorer selection in gastrocnemius muscle from the same mice as (A). **(C)** Mitochondrial interactome of down- or up-dysregulated proteins involved in mitochondrial processes in KIC gastrocnemius muscle compared to CTRL. **(C)** Heatmap representing total number of dysregulated protein (p-value<0,05, peptide>1) in gastrocnemius muscle from cancer KIC (n=5) compared to healthy CTRL (n=4) mice.

Figure S6. Cancer sarcopenic muscles demonstrate obvious mitochondria-associated protein dysregulation (related to Figure S5C).

Heatmap representing dysregulated proteins from mitochondrial interactome after MitoXplorer selection (p-value<0,05, peptide>1, log2(Foldchange)>0,5) in same gastrocnemius muscles as in Figure S5.

Figure S7 to S9. Common mitochondrial dysregulated pathways between transcriptomic and proteomic analyses (related to Figures 7 and 9)

Heatmaps corresponding to differential pathways in transcriptome (left) and proteome (right) analyses, to compare side-by-side the pathways that are similarly affected at mRNA and protein levels.

ACKNOWLEDGMENTS

We thank Marc Bartoli for recommendations in murine muscle atrophy exploration, Jérôme Robin and Arnaud Mourier for advices in isolation of active mitochondria, Sofia Vikstrom and May Sanderhoff (Seahorse/Agilent Support Scientists) for help in Seahorse experiments on isolated mitochondria, Karim Sari and Régis Vitestelle for assistance with the use of the PSEA animal housing facility, and Nuno Luis, Jérôme Avellaneda, and Frank Schnorrer for their suggestions and comments on the results. We are grateful to members of the PiCSL-FBI core facility (IBDM, AMU-Marseille, France) belonging to the France-BioImaging national research infrastructure for the electron microscopy experiments. This work benefited from equipment and services from the iGenSeq core facility (Genotyping and sequencing), at Institut du Cerveau et de la Moelle épinière (ICM, Paris, France). Proteomic analyses were performed at the mass spectrometry facility of Marseille Proteomics (marseille-proteomique.univ-amu.fr) supported by IBISA (Infrastructures Biologie Santé et Agronomie), Plateforme Technologique Aix-Marseille, the Cancéropôle PACA, the Provence-Alpes-Côte d'Azur Région, the Institut Paoli-Calmettes and the Centre de Recherche en Cancérologie de Marseille, Fonds Européen de Developpement Régional, and Plan Cancer.

This work was supported by Institut National de la Santé et de la Recherche Médicale, Centre National de la Recherche Scientifique, French Agence Nationale de la Recherche (ANR-18-CE45-0016-03 « MITODYNAMICS »). This work also benefited from grants from Cancéropôle Provence Alpes Côte d'Azur (PACA) and Fédération GEFLUC for the acquisition of the Seahorse XFe24 device. TG was supported by the ANR, and GR-C by the CONACYT (Mexico) and Ligue Nationale Contre le Cancer.

AUTHOR CONTRIBUTIONS

TG, BG, GRC, and AC planned the experiments. TG and BG performed the experiments. TG, FM, BH, BG, and AC analyzed the data. NML, JA, and FS provided expertise in muscles analyses. LC and SA were involved in mass spectrometry analysis. TG, FM, SA, BG, and AC wrote the manuscript. All authors contributed to the review and approval of the final manuscript.

COMPETING INTERESTS

The authors declare no conflicts of interests.

REFERENCES

1. Ferlay J, Colombet M, Soerjomataram I, Mathers C, Parkin DM, Pineros M, et al. Estimating the global cancer incidence and mortality in 2018: GLOBOCAN sources and methods. *Int J Cancer* 2019;**144**:1941-53.

2. Rahib L, Smith BD, Aizenberg R, Rosenzweig AB, Fleshman JM, Matrisian LM. Projecting cancer incidence and deaths to 2030: the unexpected burden of thyroid, liver, and pancreas cancers in the United States. *Cancer Res* 2014;**74**:2913-21.

3. Saad AM, Turk T, Al-Husseini MJ, Abdel-Rahman O. Trends in pancreatic adenocarcinoma incidence and mortality in the United States in the last four decades; a SEER-based study. *BMC Cancer* 2018;**18**:688.

4. Siegel RL, Miller KD, Fuchs HE, Jemal A. Cancer Statistics, 2021. *CA Cancer J Clin* 2021;**71**:7-33.

5. Nevala-Plagemann C, Hidalgo M, Garrido-Laguna I. From state-of-the-art treatments to novel therapies for advanced-stage pancreatic cancer. *Nat Rev Clin Oncol* 2020;**17**:108-23.

6. Baracos VE, Martin L, Korc M, Guttridge DC, Fearon KCH. Cancer-associated cachexia. *Nat Rev Dis Primers* 2018;**4**:17105.

7. Fearon K, Strasser F, Anker SD, Bosaeus I, Bruera E, Fainsinger RL, et al. Definition and classification of cancer cachexia: an international consensus. *Lancet Oncol* 2011;**12**:489-95.

8. Stubbins R, Bernicker EH, Quigley EMM. Cancer cachexia: a multifactoral disease that needs a multimodal approach. *Curr Opin Gastroenterol* 2020;**36**:141-6.

9. Hendifar AE, Chang JI, Huang BZ, Tuli R, Wu BU. Cachexia, and not obesity, prior to pancreatic cancer diagnosis worsens survival and is negated by chemotherapy. *J Gastrointest Oncol* 2018;**9**:17-23.

10. Mintziras I, Miligkos M, Wachter S, Manoharan J, Maurer E, Bartsch DK. Sarcopenia and sarcopenic obesity are significantly associated with poorer overall survival in patients with pancreatic cancer: Systematic review and meta-analysis. *Int J Surg* 2018;**59**:19-26.

11. Argiles JM, Busquets S, Stemmler B, Lopez-Soriano FJ. Cancer cachexia: understanding the molecular basis. *Nat Rev Cancer* 2014;**14**:754-62.

12. Argiles JM, Lopez-Soriano FJ, Busquets S. Mediators of cachexia in cancer patients. *Nutrition* 2019;**66**:11-5.

13. Biswas AK, Acharyya S. Understanding cachexia in the context of metastatic progression. *Nat Rev Cancer* 2020;**20**:274-84.

14. Argiles JM, Busquets S, Stemmler B, Lopez-Soriano FJ. Cachexia and sarcopenia: mechanisms and potential targets for intervention. *Curr Opin Pharmacol* 2015;**22**:100-6.

15. van der Ende M, Grefte S, Plas R, Meijerink J, Witkamp RF, Keijer J, et al. Mitochondrial dynamics in cancer-induced cachexia. *Biochim Biophys Acta Rev Cancer* 2018;**1870**:137-50.

16. Murphy MP, Hartley RC. Mitochondria as a therapeutic target for common pathologies. *Nat Rev Drug Discov* 2018;**17**:865-86.

17. Annesley SJ, Fisher PR. Mitochondria in Health and Disease. *Cells* 2019;**8**:

18. Russell OM, Gorman GS, Lightowlers RN, Turnbull DM. Mitochondrial Diseases: Hope for the Future. *Cell* 2020;**181**:168-88.

19. Abdel Hadi N, Reyes-Castellanos G, Carrier A. Targeting Redox Metabolism in Pancreatic Cancer. *Int J Mol Sci* 2021;**22**:1534.

20. Masoud R, Reyes-Castellanos G, Lac S, Garcia J, Dou S, Shintu L, et al. Targeting Mitochondrial Complex I Overcomes Chemoresistance in High OXPHOS Pancreatic Cancer. *Cell Rep Med* 2020;**1**:100143.

21. Reyes-Castellanos G, Masoud R, Carrier A. Mitochondrial Metabolism in PDAC: From Better Knowledge to New Targeting Strategies. *Biomedicines* 2020;**8**:270.

22. Gilabert M, Calvo E, Airoldi A, Hamidi T, Moutardier V, Turrini O, et al. Pancreatic cancer-induced cachexia is Jak2-dependent in mice. *J Cell Physiol* 2014;**229**:1437-43.

23. Michaelis KA, Zhu X, Burfeind KG, Krasnow SM, Levasseur PR, Morgan TK, et al. Establishment and characterization of a novel murine model of pancreatic cancer cachexia. *J Cachexia Sarcopenia Muscle* 2017;**8**:824-38.

24. Zhu X, Burfeind KG, Michaelis KA, Braun TP, Olson B, Pelz KR, et al. MyD88 signalling is critical in the development of pancreatic cancer cachexia. *J Cachexia Sarcopenia Muscle* 2019;**10**:378-90.

25. Kemp GJ, Ahmad RE, Nicolay K, Prompers JJ. Quantification of skeletal muscle mitochondrial function by 31P magnetic resonance spectroscopy techniques: a quantitative review. *Acta Physiol (Oxf)* 2015;**213**:107-44.

26. Prompers JJ, Wessels B, Kemp GJ, Nicolay K. MITOCHONDRIA: investigation of in vivo muscle mitochondrial function by 31P magnetic resonance spectroscopy. *Int J Biochem Cell Biol* 2014;**50**:67-72.

27. Johns N, Stephens NA, Fearon KC. Muscle wasting in cancer. *Int J Biochem Cell Biol* 2013;**45**:2215-29.

28. VanderVeen BN, Fix DK, Carson JA. Disrupted Skeletal Muscle Mitochondrial Dynamics, Mitophagy, and Biogenesis during Cancer Cachexia: A Role for Inflammation. *Oxid Med Cell Longev* 2017;**2017**:3292087.

29. Bulthuis EP, Adjobo-Hermans MJW, Willems P, Koopman WJH. Mitochondrial Morphofunction in Mammalian Cells. *Antioxid Redox Signal* 2019;**30**:2066-109.

30. Gomes LC, Di Benedetto G, Scorrano L. During autophagy mitochondria elongate, are spared from degradation and sustain cell viability. *Nat Cell Biol* 2011;**13**:589-98.

31. Penna F, Ballaro R, Costelli P. The Redox Balance: A Target for Interventions Against Muscle Wasting in Cancer Cachexia? *Antioxid Redox Signal* 2020;**33**:542-58.

32. Fukawa T, Yan-Jiang BC, Min-Wen JC, Jun-Hao ET, Huang D, Qian CN, et al. Excessive fatty acid oxidation induces muscle atrophy in cancer cachexia. *Nat Med* 2016;**22**:666-71.

33. Barbieri E, Agostini D, Polidori E, Potenza L, Guescini M, Lucertini F, et al. The pleiotropic effect of physical exercise on mitochondrial dynamics in aging skeletal muscle. *Oxid Med Cell Longev* 2015;**2015**:917085.

34. Rygiel KA, Picard M, Turnbull DM. The ageing neuromuscular system and sarcopenia: a mitochondrial perspective. *J Physiol* 2016;**594**:4499-512.

35. Liu Y, Beyer A, Aebersold R. On the Dependency of Cellular Protein Levels on mRNA Abundance. *Cell* 2016;**165**:535-50.

36. Piccirillo CA, Bjur E, Topisirovic I, Sonenberg N, Larsson O. Translational control of immune responses: from transcripts to translatomes. *Nat Immunol* 2014;**15**:503-11.

37. de Castro GS, Simoes E, Lima J, Ortiz-Silva M, Festuccia WT, Tokeshi F, et al. Human Cachexia Induces Changes in Mitochondria, Autophagy and Apoptosis in the Skeletal Muscle. *Cancers (Basel)* 2019;**11**:

38. Zhong X, Narasimhan A, Silverman LM, Young AR, Shahda S, Liu S, et al. Sex specificity of pancreatic cancer cachexia phenotypes, mechanisms, and treatment in mice and humans: role of Activin. *J Cachexia Sarcopenia Muscle* 2022;

39. Waltz TB, Fivenson EM, Morevati M, Li C, Becker KG, Bohr VA, et al. Sarcopenia, Aging and Prospective Interventional Strategies. *Curr Med Chem* 2018;**25**:5588-96.

40. Alway SE, Mohamed JS, Myers MJ. Mitochondria Initiate and Regulate Sarcopenia. *Exerc Sport Sci Rev* 2017;**45**:58-69.

41. Brown JL, Rosa-Caldwell ME, Lee DE, Blackwell TA, Brown LA, Perry RA, et al. Mitochondrial degeneration precedes the development of muscle atrophy in progression of cancer cachexia in tumour-bearing mice. *J Cachexia Sarcopenia Muscle* 2017;**8**:926-38.

42. Giannesini B, Vilmen C, Le Fur Y, Dalmasso C, Cozzone PJ, Bendahan D. A strictly noninvasive MR setup dedicated to longitudinal studies of mechanical performance, bioenergetics, anatomy, and muscle recruitment in contracting mouse skeletal muscle. *Magn Reson Med* 2010;**64**:262-70.

43. Vanhamme L, van den Boogaart A, Van Huffel S. Improved method for accurate and efficient quantification of MRS data with use of prior knowledge. *J Magn Reson* 1997;**129**:35-43.

44. Al Tanoury Z, Zimmerman JF, Rao J, Sieiro D, McNamara HM, Cherrier T, et al. Prednisolone rescues Duchenne muscular dystrophy phenotypes in human pluripotent stem cell-derived skeletal muscle in vitro. *Proc Natl Acad Sci U S A* 2021;**118**:

45. Shevchenko A, Wilm M, Vorm O, Mann M. Mass spectrometric sequencing of proteins silver-stained polyacrylamide gels. *Anal Chem* 1996;**68**:850-8.

46. Cox J, Hein MY, Luber CA, Paron I, Nagaraj N, Mann M. Accurate proteome-wide label-free quantification by delayed normalization and maximal peptide ratio extraction, termed MaxLFQ. *Mol Cell Proteomics* 2014;**13**:2513-26.

47. Cox J, Mann M. MaxQuant enables high peptide identification rates, individualized p.p.b.-range mass accuracies and proteome-wide protein quantification. *Nat Biotechnol* 2008;**26**:1367-72.

48. Cox J, Neuhauser N, Michalski A, Scheltema RA, Olsen JV, Mann M. Andromeda: a peptide search engine integrated into the MaxQuant environment. *J Proteome Res* 2011;**10**:1794-805.

49. Tusher VG, Tibshirani R, Chu G. Significance analysis of microarrays applied to the ionizing radiation response. *Proc Natl Acad Sci U S A* 2001;**98**:5116-21.

50. Tyanova S, Temu T, Sinitcyn P, Carlson A, Hein MY, Geiger T, et al. The Perseus computational platform for comprehensive analysis of (prote)omics data. *Nat Methods* 2016;**13**:731-40.

51. Yim A, Koti P, Bonnard A, Marchiano F, Durrbaum M, Garcia-Perez C, et al. mitoXplorer, a visual data mining platform to systematically analyze and visualize mitochondrial expression dynamics and mutations. *Nucleic Acids Res* 2020;**48**:605-32.

52. Deutsch EW, Bandeira N, Sharma V, Perez-Riverol Y, Carver JJ, Kundu DJ, et al. The ProteomeXchange consortium in 2020: enabling 'big data' approaches in proteomics. *Nucleic Acids Res* 2020;**48**:D1145-D52.

53. Perez-Riverol Y, Csordas A, Bai J, Bernal-Llinares M, Hewapathirana S, Kundu DJ, et al. The PRIDE database and related tools and resources in 2019: improving support for quantification data. *Nucleic Acids Res* 2019;**47**:D442-D50.

Figure 1

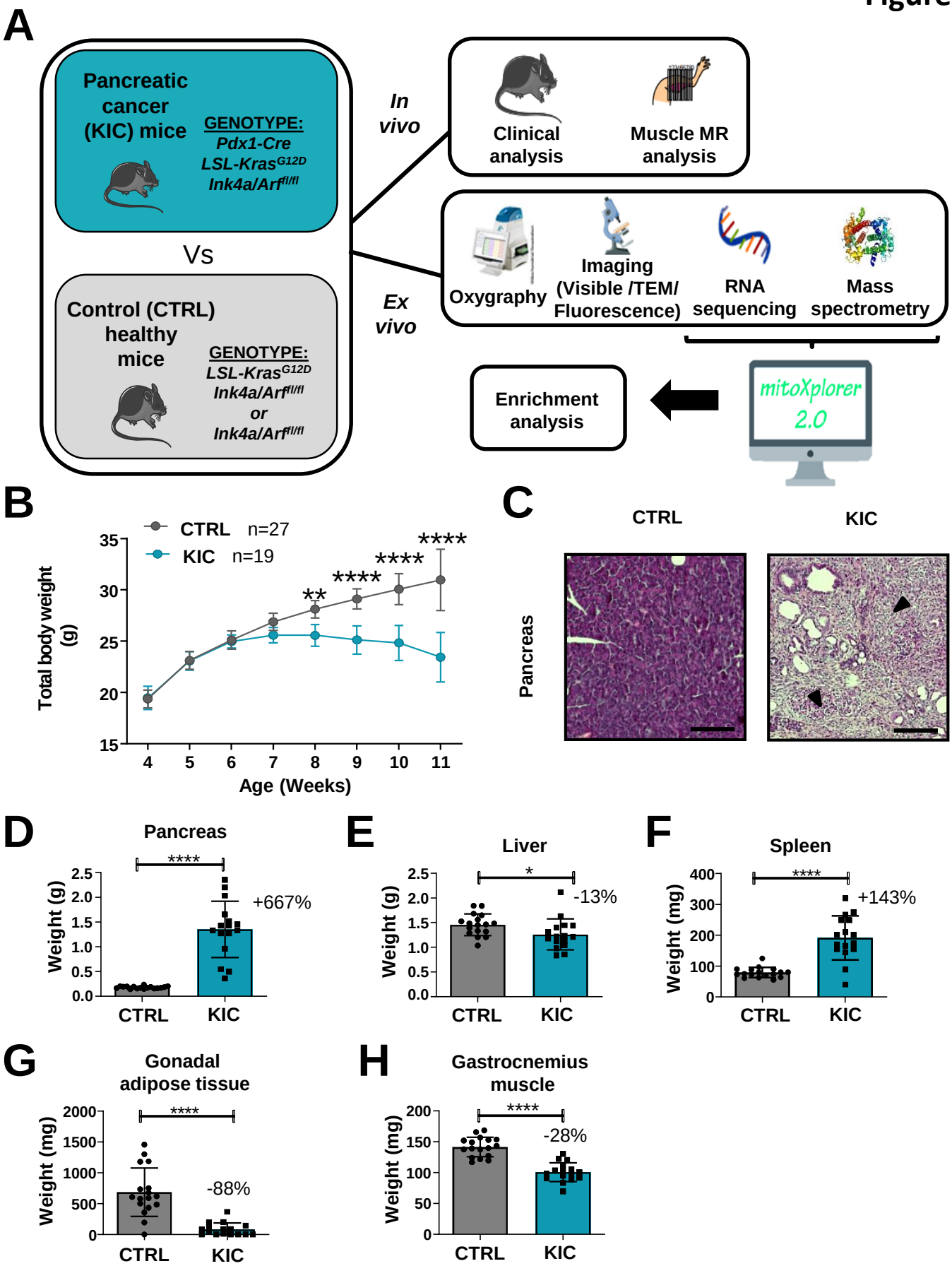
A
Pancreatic cancer (KIC) mice
GENOTYPE:
Pdx1-Cre
LSL-KrasG12D
Ink4a/Arffl/fl
Vs
Control (CTRL) healthy mice
GENOTYPE:
LSL-KrasG12D
Ink4a/Arffl/fl
or
Ink4a/Arffl/fl
In vivo
Clinical analysis
Muscle MR analysis
Ex vivo
Oxygraphy
Imaging (Visible /TEM/ Fluorescence)
RNA sequencing
Mass spectrometry
mitoXplorer 2.0
Enrichment analysis
B
CTRL n=27
KIC n=19
Total body weight (g)
Age (Weeks)
C
CTRL
KIC
Pancreas
D
Pancreas
Weight (g)
+667%
E
Liver
Weight (g)
-13%
F
Spleen
Weight (mg)
+143%
G
Gonadal adipose tissue
Weight (mg)
-88%
H
Gastrocnemius muscle
Weight (mg)
-28%
CTRL
KIC

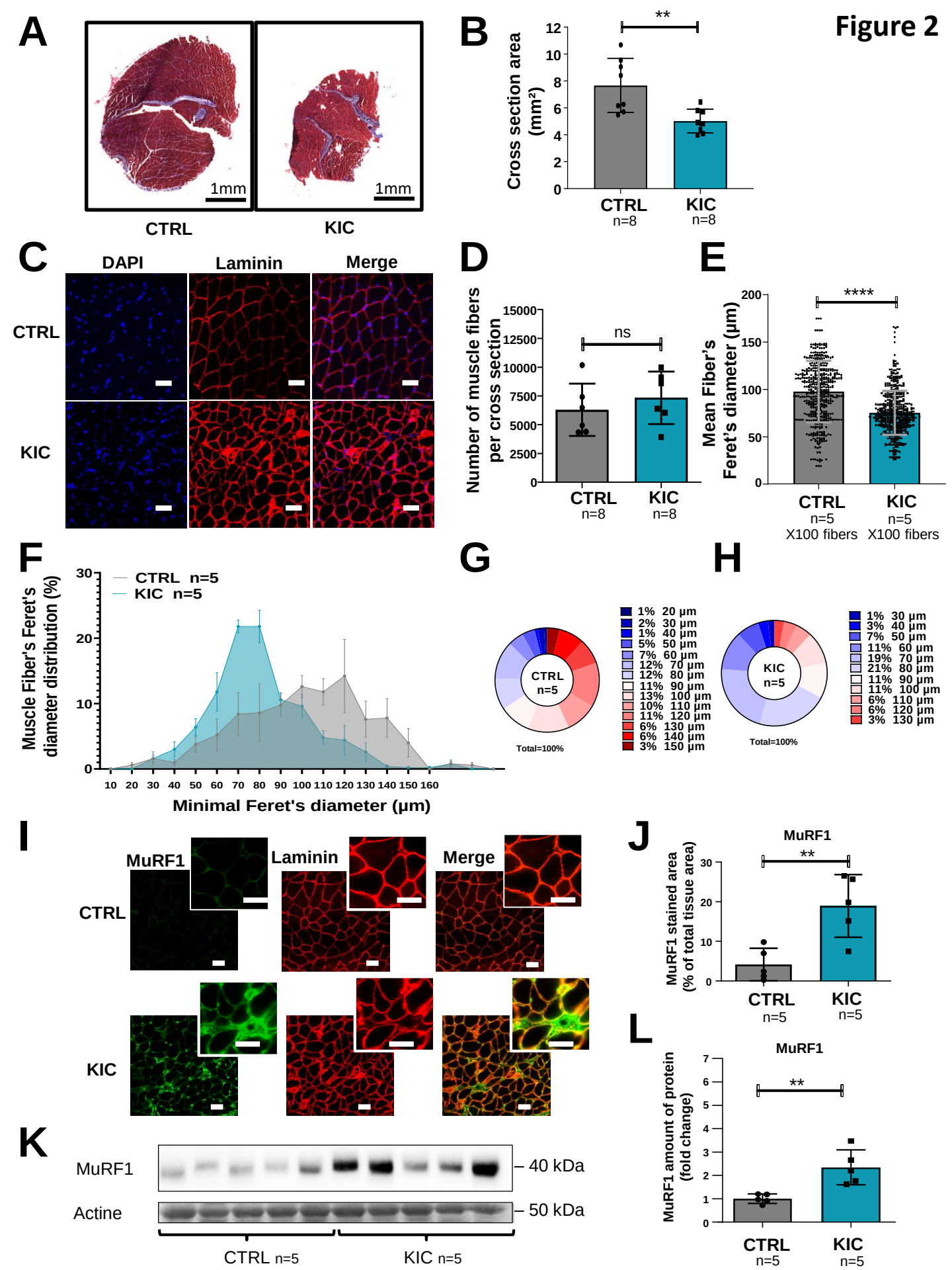
Figure 2
A
1mm
1mm
CTRL
KIC
B
Cross section area (mm²)
**
CTRL n=8
KIC n=8
C
DAPI
Laminin
Merge
CTRL
KIC
D
Number of muscle fibers per cross section
ns
CTRL n=8
KIC n=8
E
Mean Fiber's Feret's diameter (µm)
****
CTRL n=5 X100 fibers
KIC n=5 X100 fibers
F
Muscle Fiber's Feret's diameter distribution (%)
CTRL n=5
KIC n=5
Minimal Feret's diameter (µm)
G
CTRL n=5
Total=100%
1% 20 µm
2% 30 µm
1% 40 µm
5% 50 µm
7% 60 µm
12% 70 µm
12% 80 µm
11% 90 µm
13% 100 µm
10% 110 µm
11% 120 µm
6% 130 µm
6% 140 µm
3% 150 µm
H
KIC n=5
Total=100%
1% 30 µm
3% 40 µm
7% 50 µm
11% 60 µm
19% 70 µm
21% 80 µm
11% 90 µm
11% 100 µm
6% 110 µm
6% 120 µm
3% 130 µm
I
MuRF1
Laminin
Merge
CTRL
KIC
J
MuRF1
MuRF1 stained area (% of total tissue area)
**
CTRL n=5
KIC n=5
L
MuRF1
MuRF1 amount of protein (fold change)
**
CTRL n=5
KIC n=5
K
MuRF1
Actine
40 kDa
50 kDa
CTRL n=5
KIC n=5

Figure 3

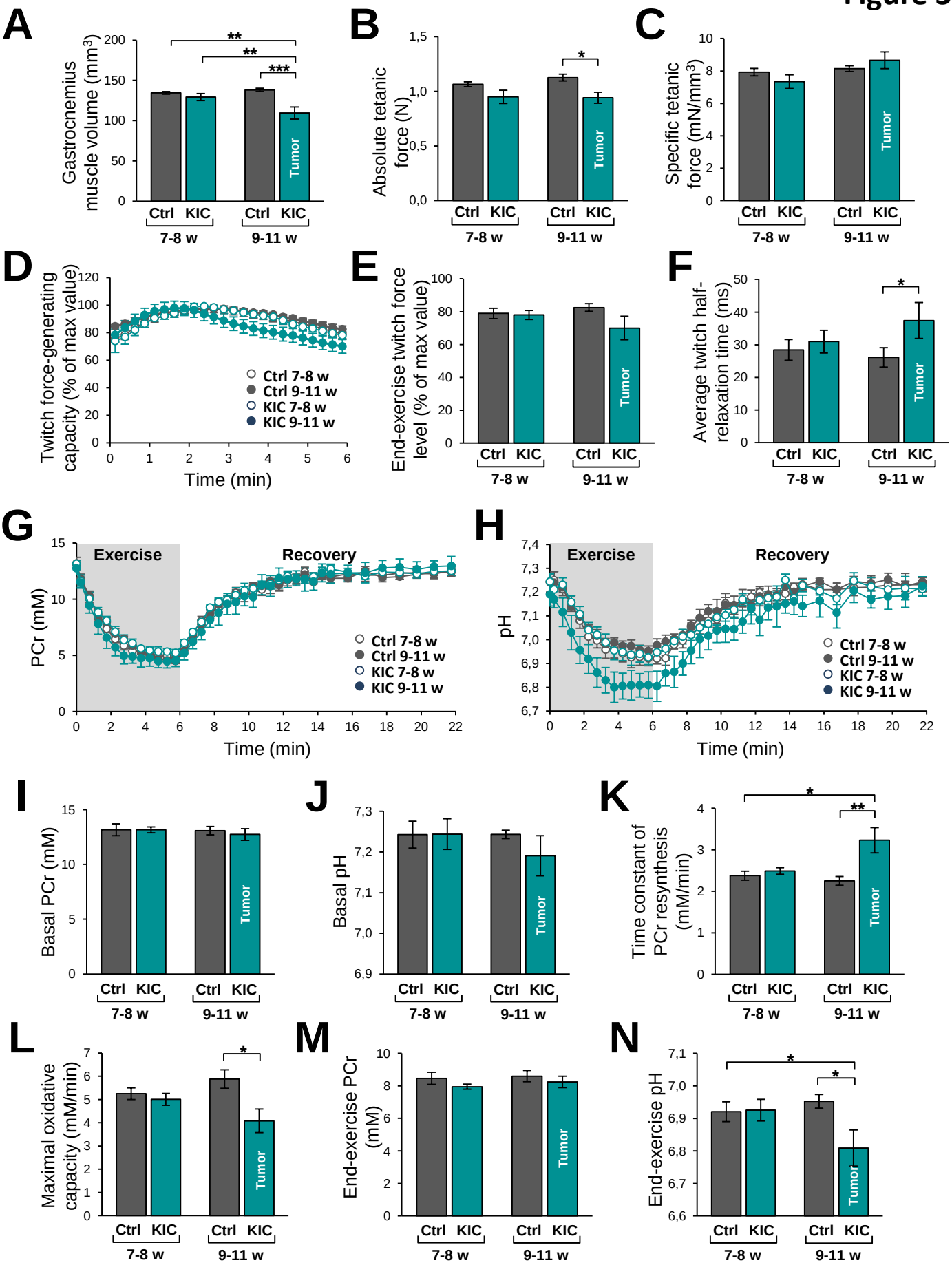
A
Gastrocnemius muscle volume (mm³)
200
150
100
50
0
**
**
***
Tumor
Ctrl KIC Ctrl KIC
7-8 w 9-11 w
B
Absolute tetanic force (N)
1,5
1,0
0,5
0,0
*
Tumor
Ctrl KIC Ctrl KIC
7-8 w 9-11 w
C
Specific tetanic force (mN/mm³)
10
8
6
4
2
0
Tumor
Ctrl KIC Ctrl KIC
7-8 w 9-11 w
D
Twitch force-generating capacity (% of max value)
120
100
80
60
40
20
0
0 1 2 3 4 5 6
Time (min)
Ctrl 7-8 w
Ctrl 9-11 w
KIC 7-8 w
KIC 9-11 w
E
End-exercise twitch force level (% of max value)
100
80
60
40
20
0
Tumor
Ctrl KIC Ctrl KIC
7-8 w 9-11 w
F
Average twitch half-relaxation time (ms)
50
40
30
20
10
0
*
Tumor
Ctrl KIC Ctrl KIC
7-8 w 9-11 w
G
PCr (mM)
15
10
5
0
Exercise
Recovery
0 2 4 6 8 10 12 14 16 18 20 22
Time (min)
Ctrl 7-8 w
Ctrl 9-11 w
KIC 7-8 w
KIC 9-11 w
H
pH
7,4
7,3
7,2
7,1
7,0
6,9
6,8
6,7
Exercise
Recovery
0 2 4 6 8 10 12 14 16 18 20 22
Time (min)
Ctrl 7-8 w
Ctrl 9-11 w
KIC 7-8 w
KIC 9-11 w
I
Basal PCr (mM)
15
10
5
0
Tumor
Ctrl KIC Ctrl KIC
7-8 w 9-11 w
J
Basal pH
7,3
7,2
7,1
7,0
6,9
Tumor
Ctrl KIC Ctrl KIC
7-8 w 9-11 w
K
Time constant of PCr resynthesis (mM/min)
4
3
2
1
0
*
**
Tumor
Ctrl KIC Ctrl KIC
7-8 w 9-11 w
L
Maximal oxidative capacity (mM/min)
7
6
5
4
3
2
1
0
*
Tumor
Ctrl KIC Ctrl KIC
7-8 w 9-11 w
M
End-exercise PCr (mM)
10
8
6
4
2
0
Tumor
Ctrl KIC Ctrl KIC
7-8 w 9-11 w
N
End-exercise pH
7,1
7,0
6,9
6,8
6,7
6,6
*
*
Tumor
Ctrl KIC Ctrl KIC
7-8 w 9-11 w

Figure 4

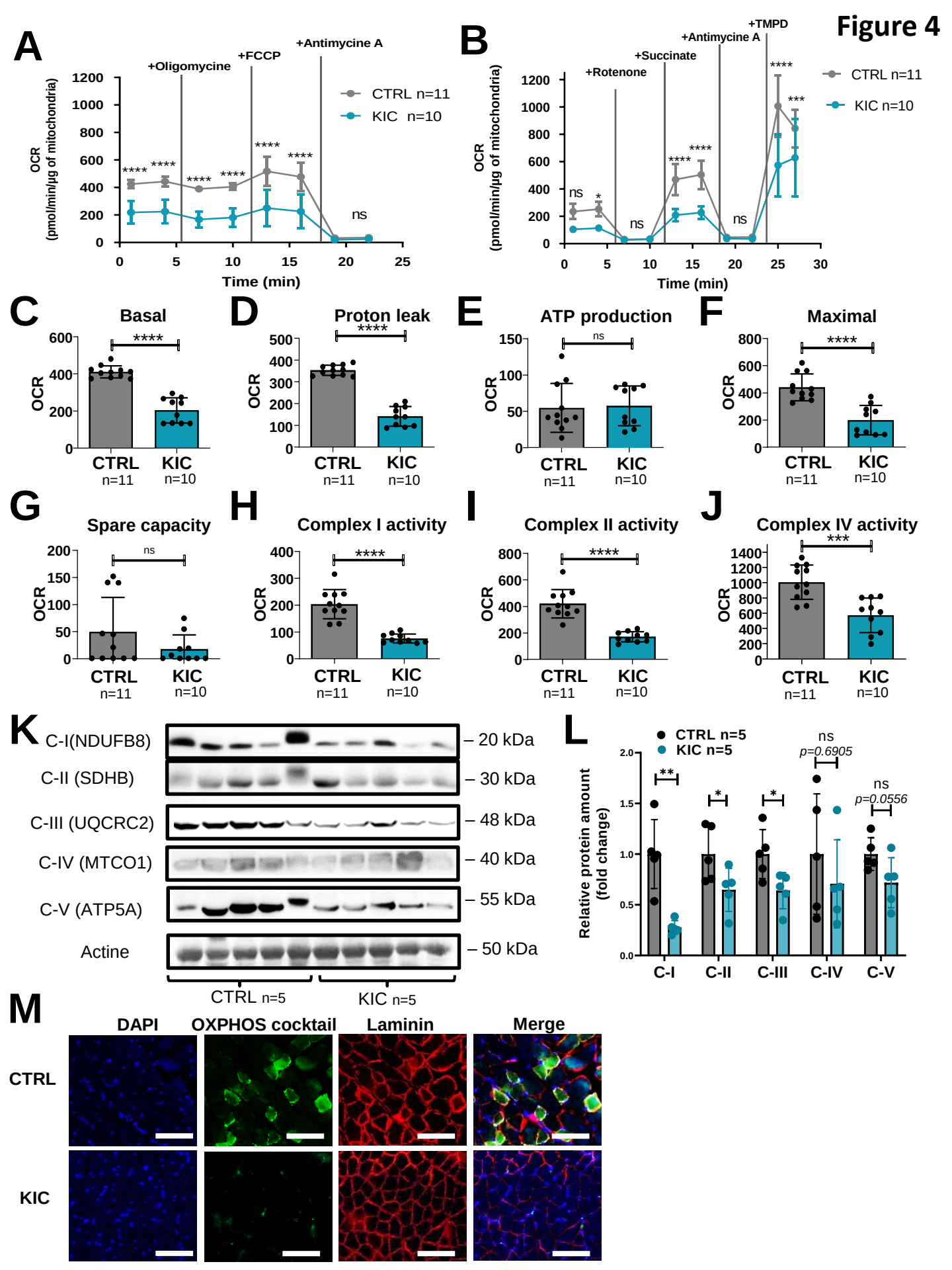
A
+Oligomycine
+FCCP
+Antimycine A
CTRL n=11
KIC n=10
OCR (pmol/min/µg of mitochondria)
Time (min)
B
+Rotenone
+Succinate
+Antimycine A
+TMPD
C Basal
D Proton leak
E ATP production
F Maximal
G Spare capacity
H Complex I activity
I Complex II activity
J Complex IV activity
OCR
CTRL n=11
KIC n=10
K
C-I(NDUFB8)
C-II (SDHB)
C-III (UQCRC2)
C-IV (MTCO1)
C-V (ATP5A)
Actine
– 20 kDa
– 30 kDa
– 48 kDa
– 40 kDa
– 55 kDa
– 50 kDa
CTRL n=5
KIC n=5
L
CTRL n=5
KIC n=5
Relative protein amount (fold change)
p=0.6905
p=0.0556
C-I
C-II
C-III
C-IV
C-V
M
DAPI
OXPHOS cocktail
Laminin
Merge
CTRL
KIC

Figure 5

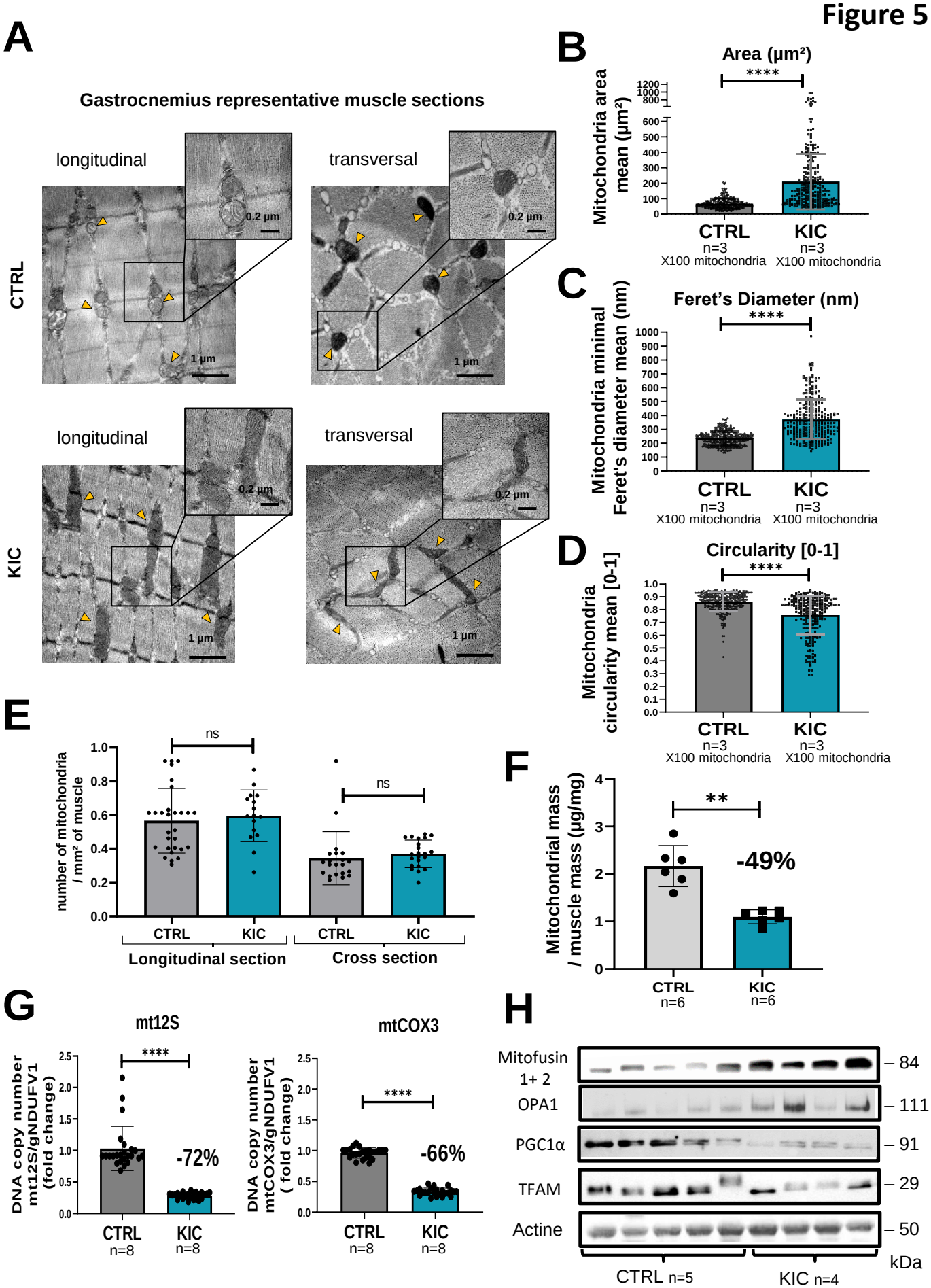
A
Gastrocnemius representative muscle sections
longitudinal
transversal
CTRL
KIC
0.2 µm
1 µm
B
Area (µm²)
Mitochondria area mean (µm²)
****
CTRL
KIC
n=3
X100 mitochondria
C
Feret's Diameter (nm)
Mitochondria minimal Feret's diameter mean (nm)
D
Circularity [0-1]
Mitochondria circularity mean [0-1]
E
number of mitochondria / mm² of muscle
ns
Longitudinal section
Cross section
F
Mitochondrial mass / muscle mass (µg/mg)
**
-49%
n=6
G
mt12S
mtCOX3
DNA copy number mt12S/gNDUFV1 (fold change)
DNA copy number mtCOX3/gNDUFV1 (fold change)
-72%
-66%
n=8
H
Mitofusin 1+ 2
OPA1
PGC1α
TFAM
Actine
84
111
91
29
50
kDa
CTRL n=5
KIC n=4

Figure 6

TRANSCRIPTOME

General dysregulated pathways from total dysregulated genes (2304)

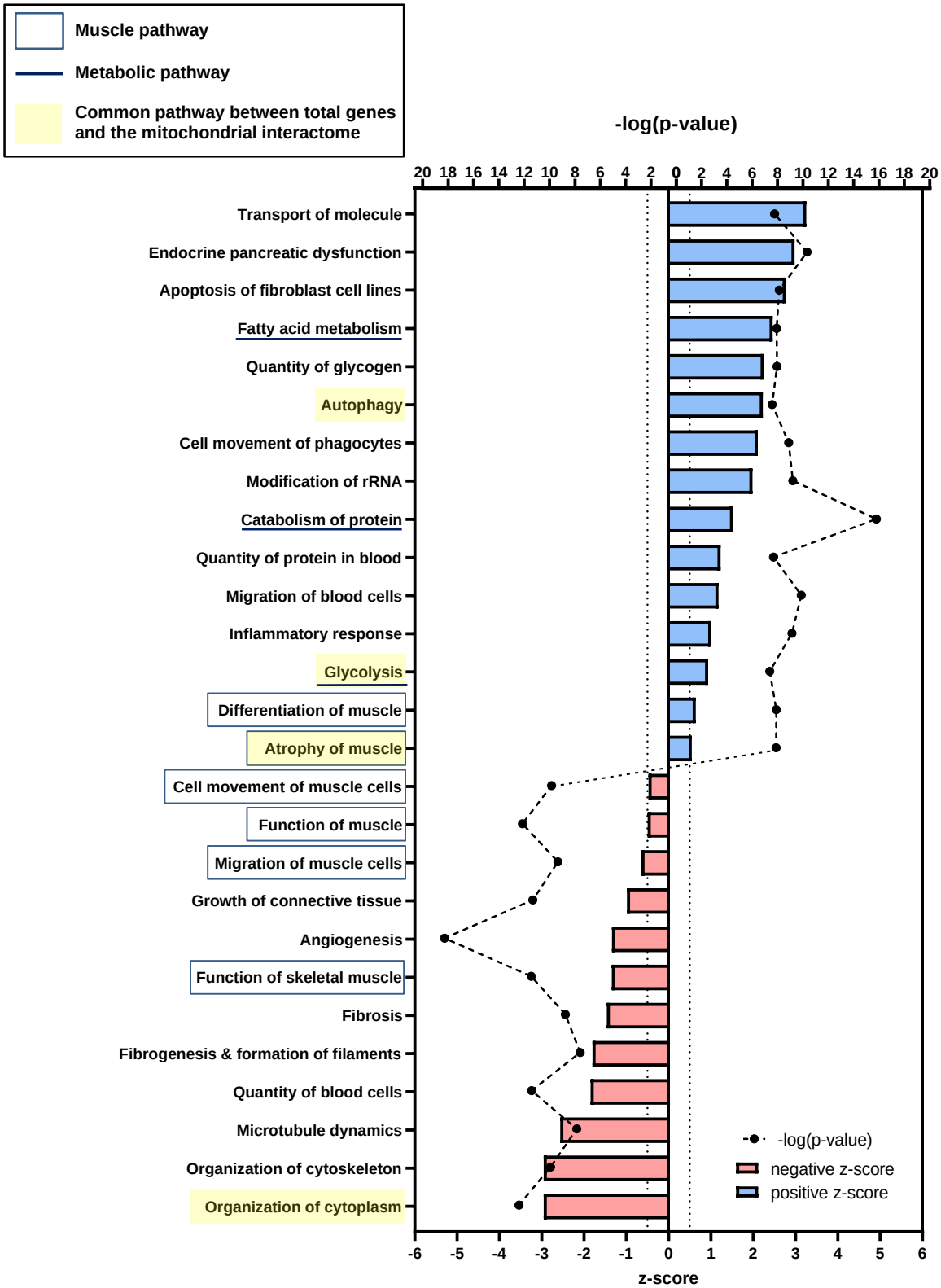

Figure 7

TRANSCRIPTOME

Mitochondrial dysregulated pathways from mitochondrial interactome dysregulated genes (178)

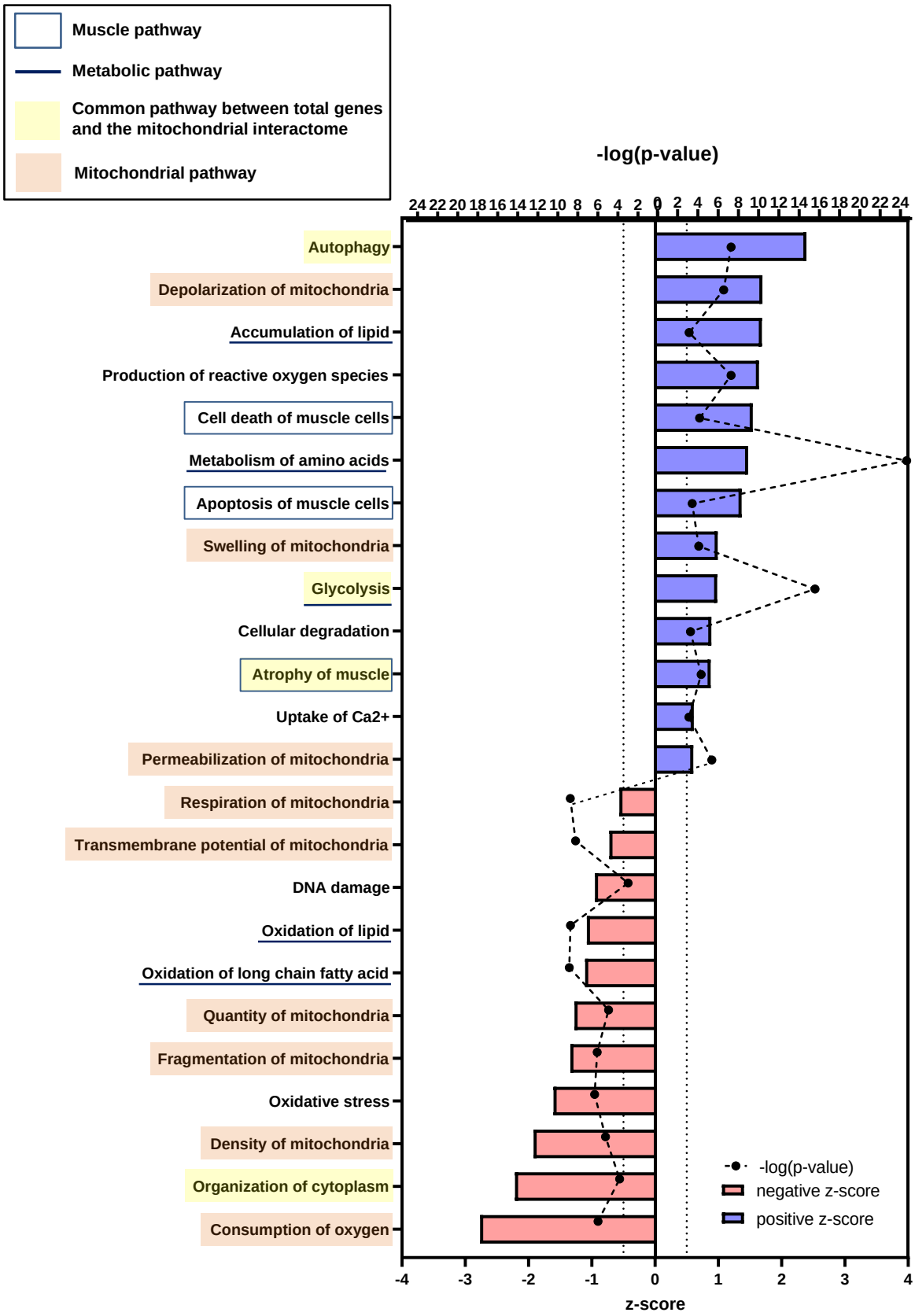

Figure 8

PROTEOME

General dysregulated pathways from total dysregulated proteins (154)

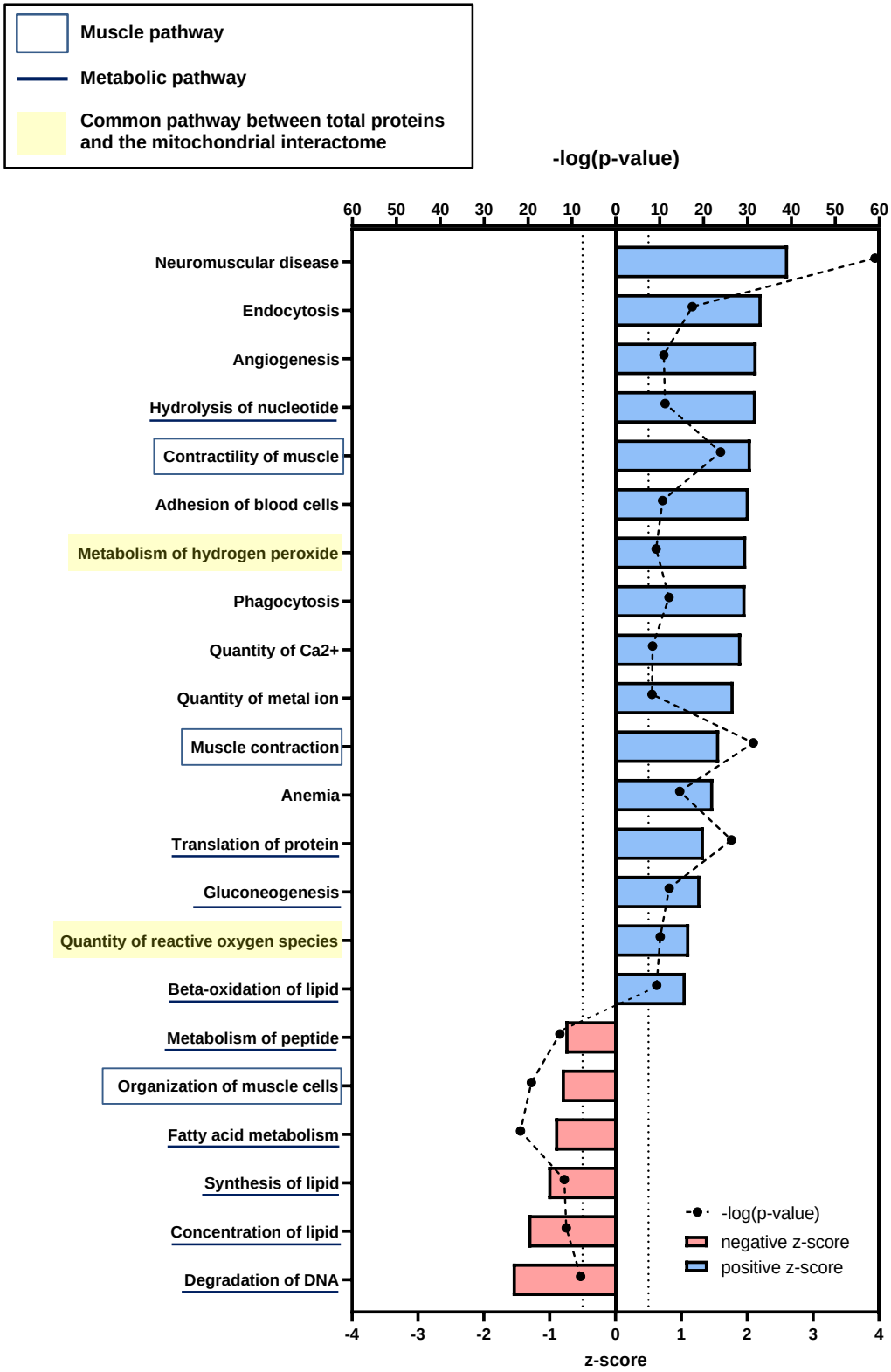

Figure 9

PROTEOME

Mitochondrial dysregulated pathways from mitochondrial interactome dysregulated proteins (70)

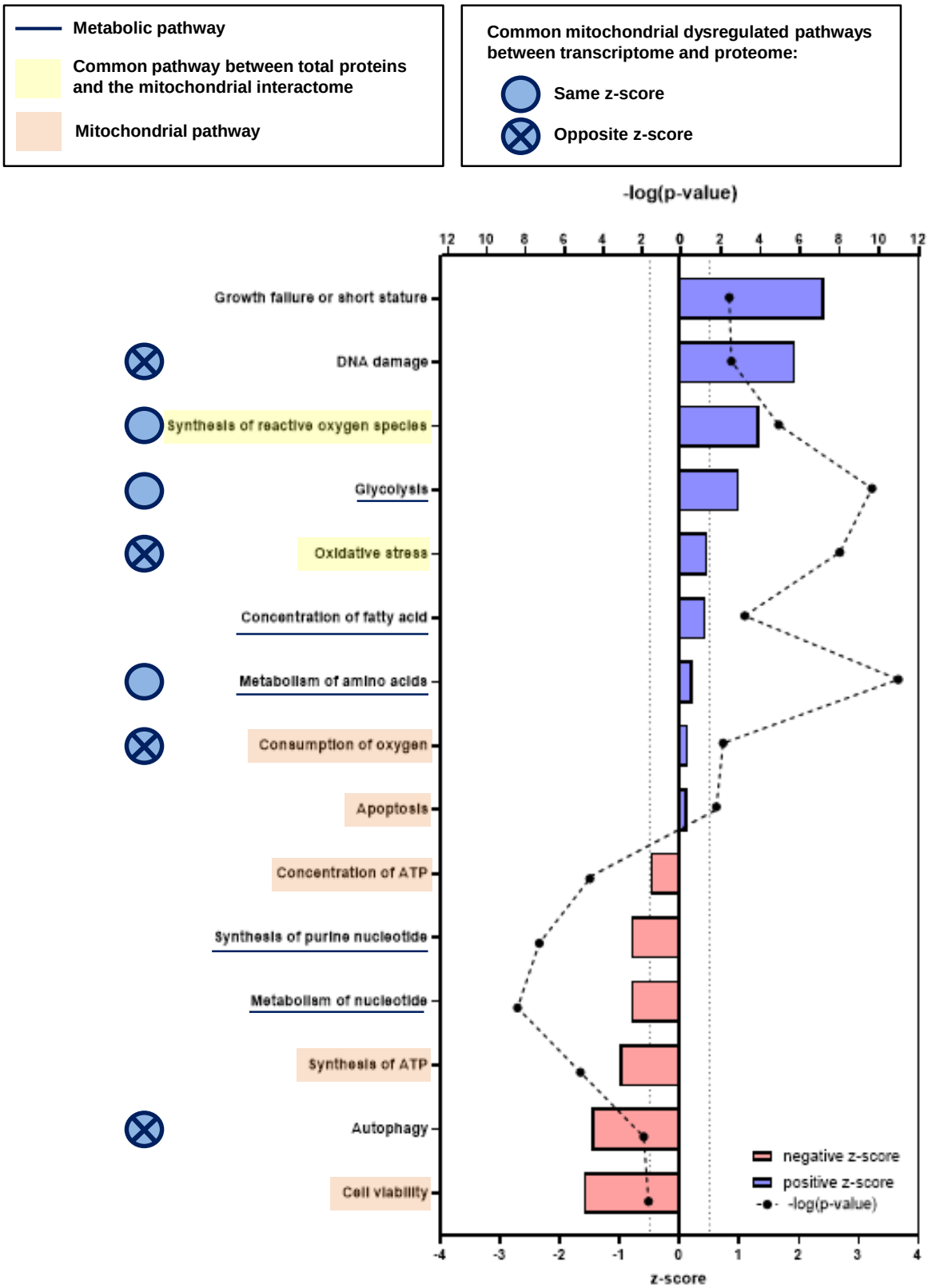

Figure S1

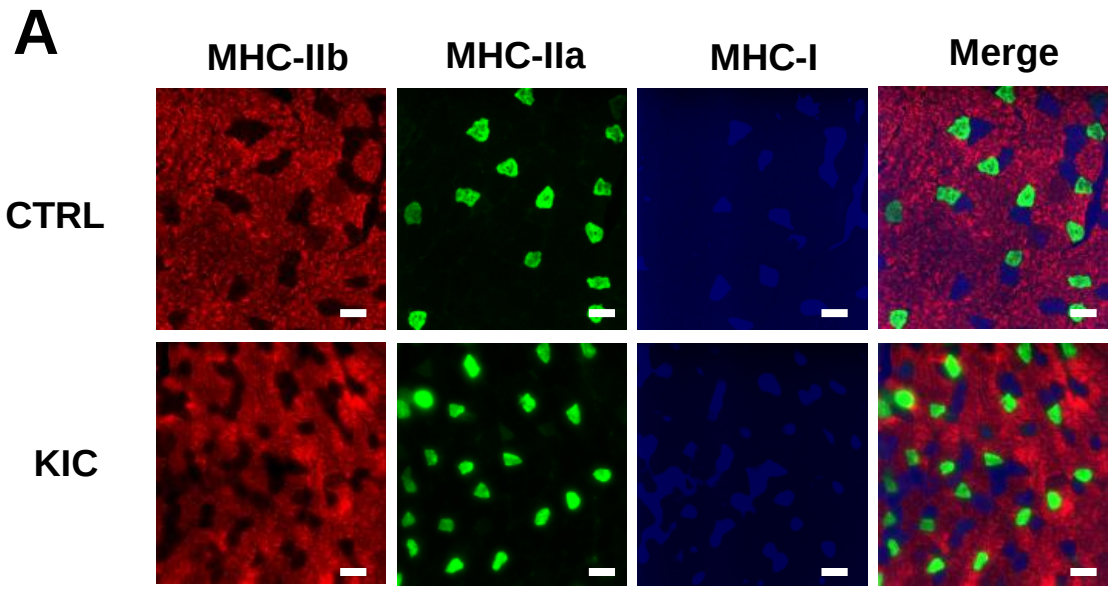
A
MHC-IIb
MHC-IIa
MHC-I
Merge
CTRL
KIC

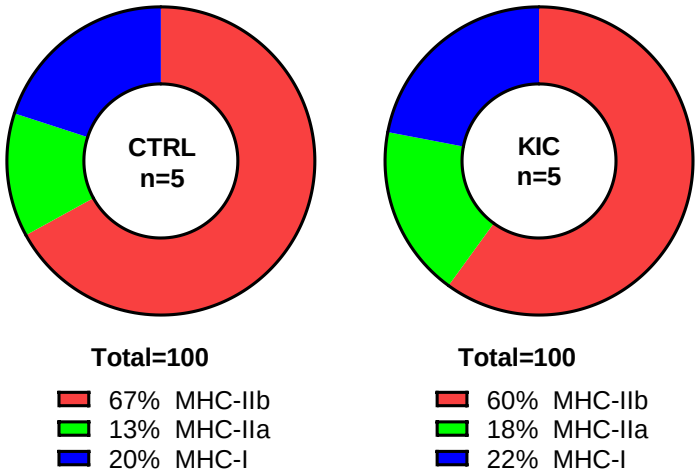
B
CTRL
n=5
KIC
n=5
Total=100
67% MHC-IIb
13% MHC-IIa
20% MHC-I
Total=100
60% MHC-IIb
18% MHC-IIa
22% MHC-I

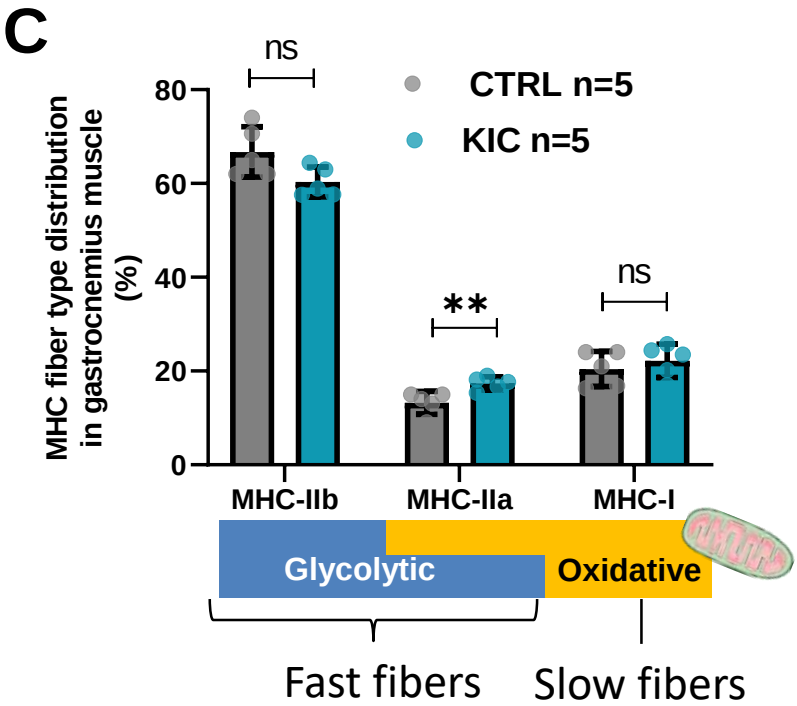
C
MHC fiber type distribution in gastrocnemius muscle (%)
80
60
40
20
0
ns
**
ns
CTRL n=5
KIC n=5
MHC-IIb
MHC-IIa
MHC-I
Glycolytic
Oxidative
Fast fibers
Slow fibers

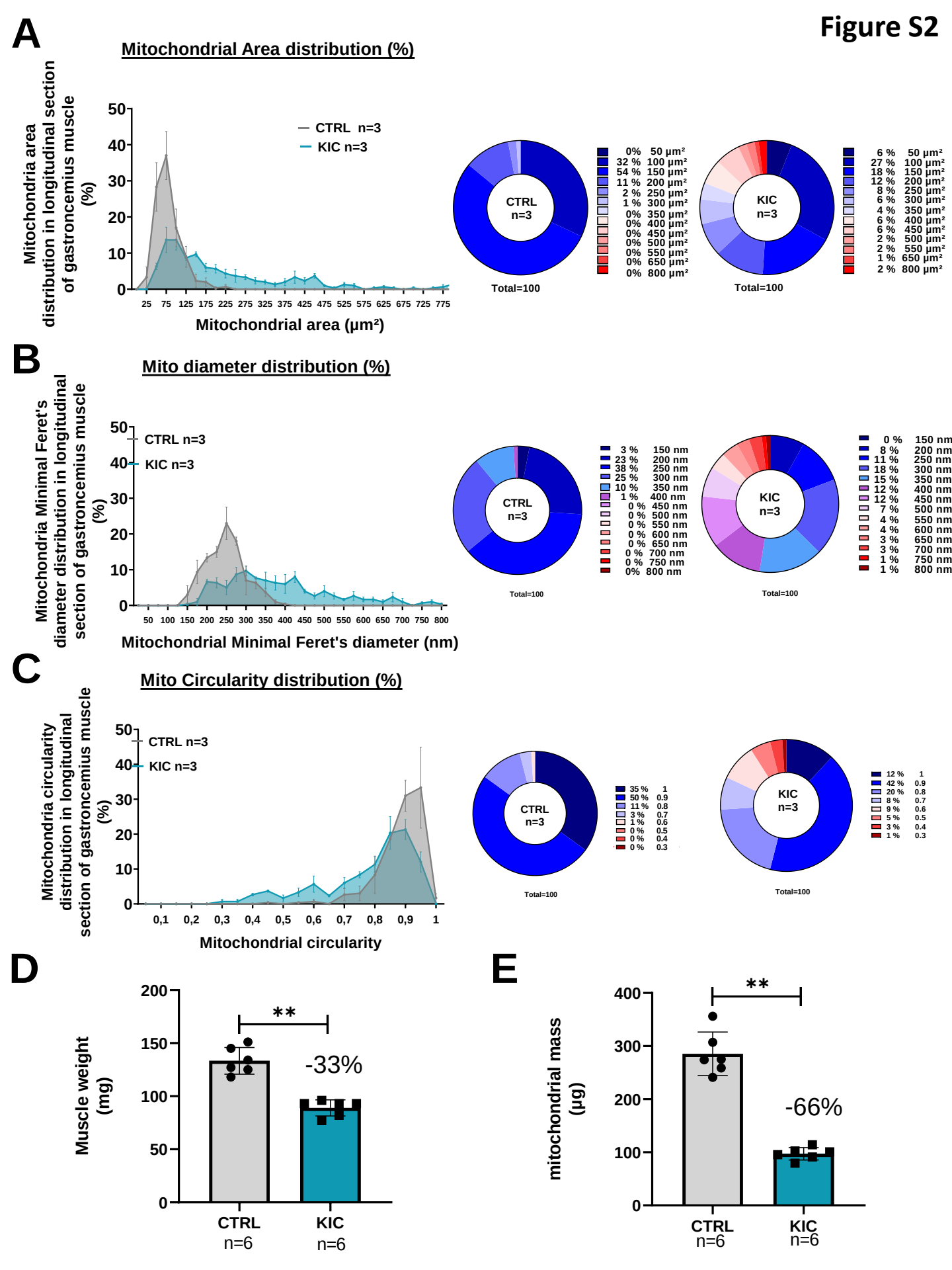
Figure S2
A
Mitochondrial Area distribution (%)
Mitochondria area distribution in longitudinal section of gastroncemius muscle (%)
CTRL n=3
KIC n=3
Mitochondrial area (µm²)
CTRL n=3
Total=100
KIC n=3
Total=100
B
Mito diameter distribution (%)
Mitochondria Minimal Feret's diameter distribution in longitudinal section of gastroncemius muscle (%)
CTRL n=3
KIC n=3
Mitochondrial Minimal Feret's diameter (nm)
CTRL n=3
Total=100
KIC n=3
Total=100
C
Mito Circularity distribution (%)
Mitochondria circularity distribution in longitudinal section of gastroncemius muscle (%)
CTRL n=3
KIC n=3
Mitochondrial circularity
CTRL n=3
Total=100
KIC n=3
Total=100
D
Muscle weight (mg)
**
-33%
CTRL n=6
KIC n=6
E
mitochondrial mass (µg)
**
-66%
CTRL n=6
KIC n=6

Figure S3

TRANSCRIPTOME

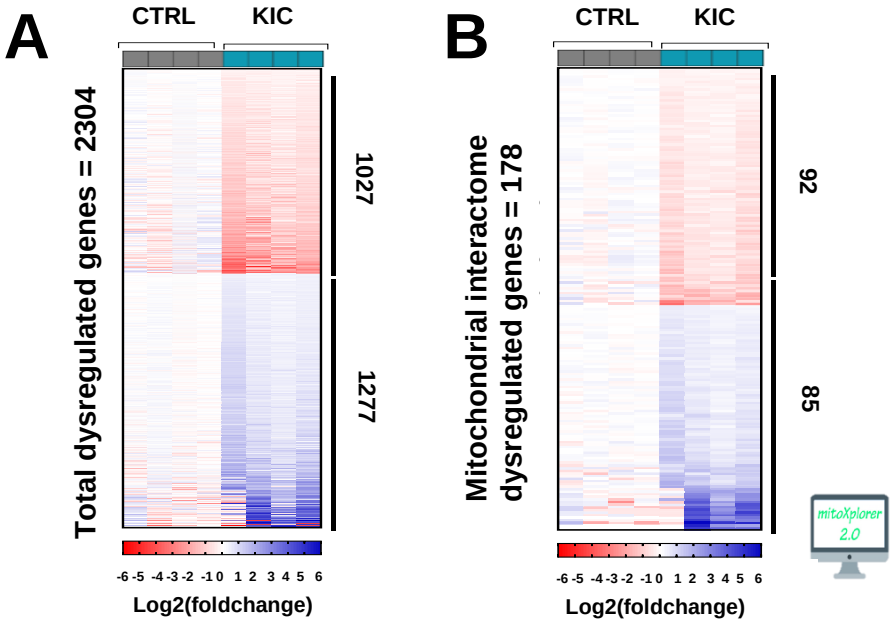

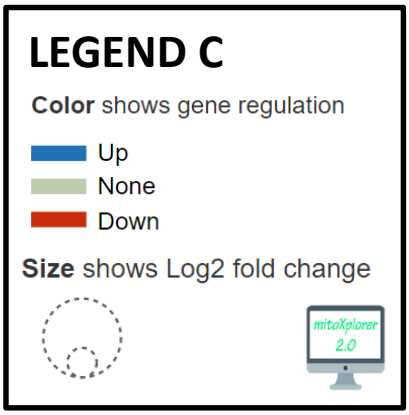

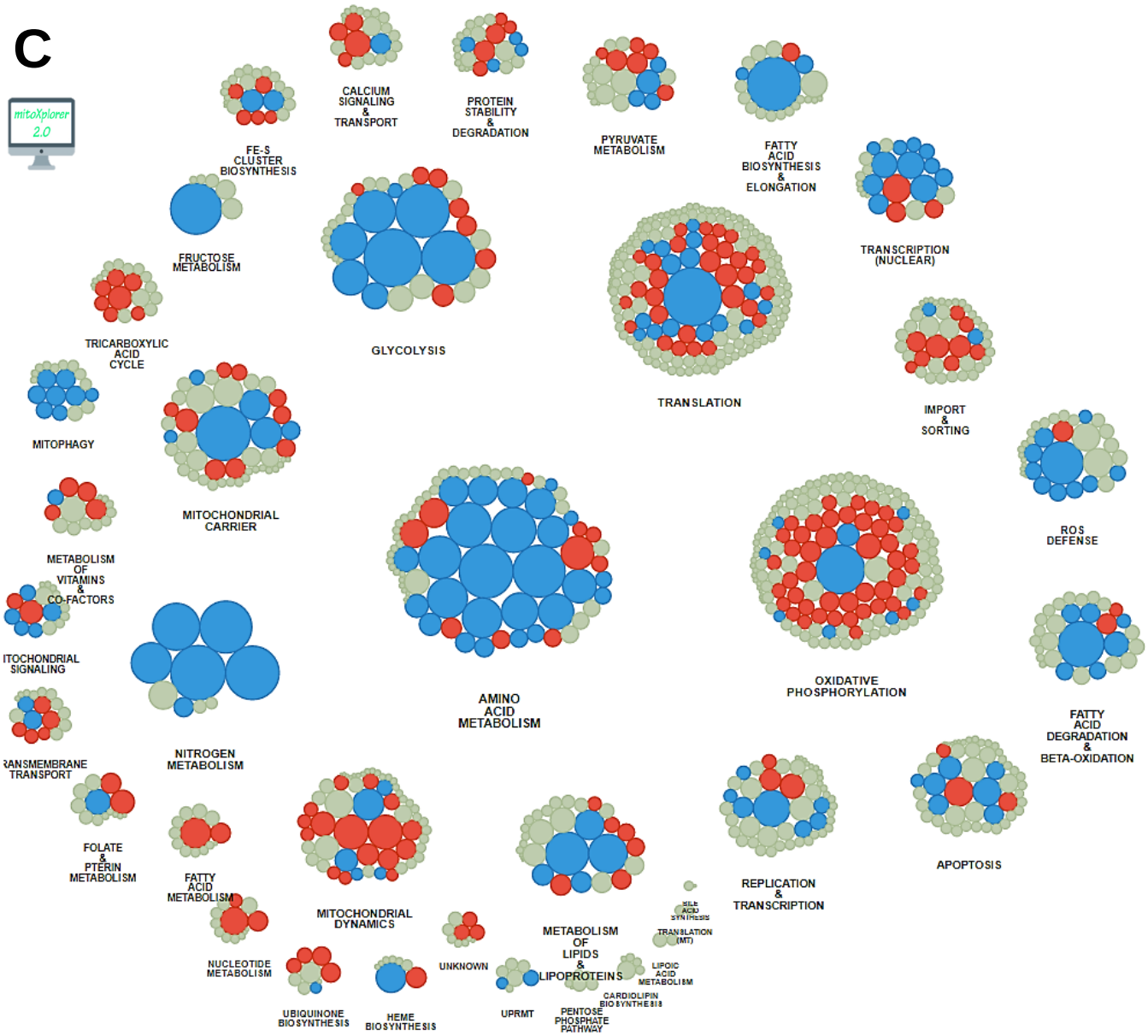

Figure S4

TRANSCRIPTOME

mitoXplorer 2.0

LEGEND

Gastrocnemius muscle

- Healthy CTRL ♂ (n=4)
- Cancer KIC ♂ (n=4)

Significance

- p<0.05
- 0.05<p<0.01
- 0.01<p<0.001

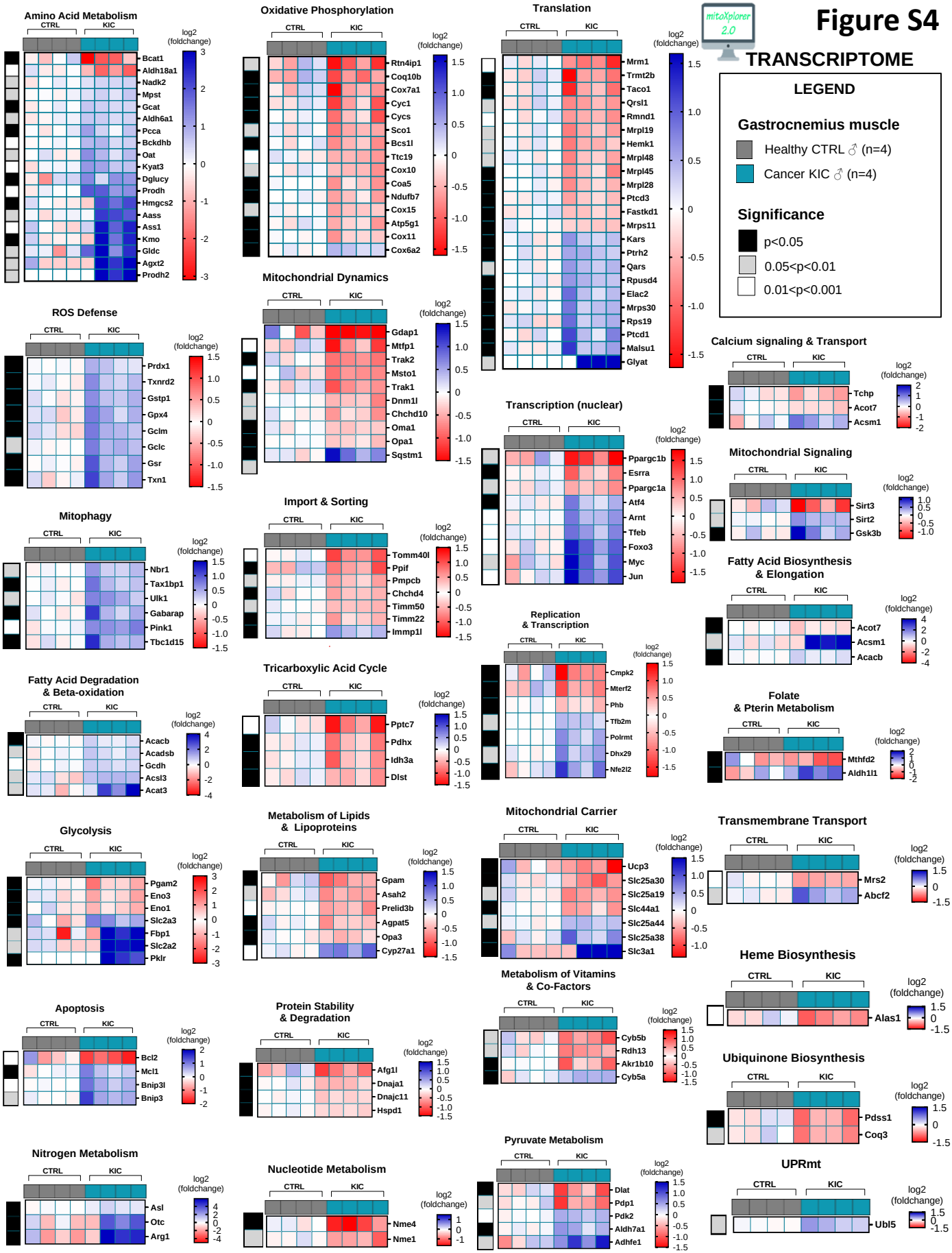

Figure S5

PROTEOME

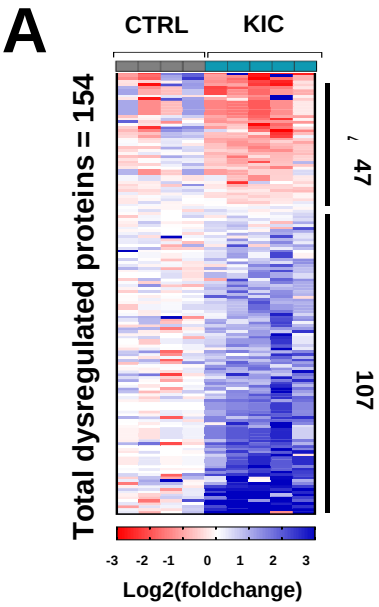

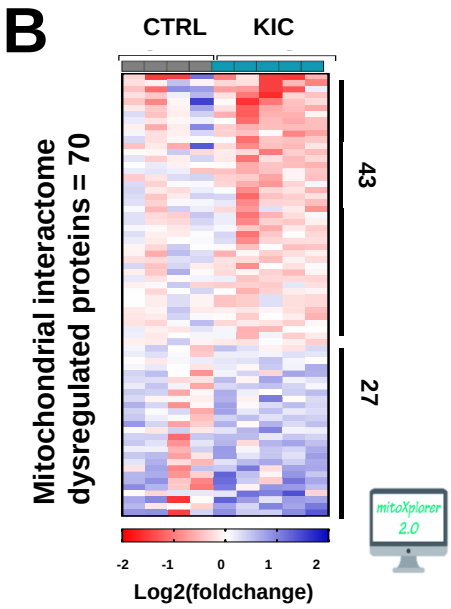

LEGEND C

Color shows protein regulation

- Up
- None
- Down

Size shows Log2 fold change

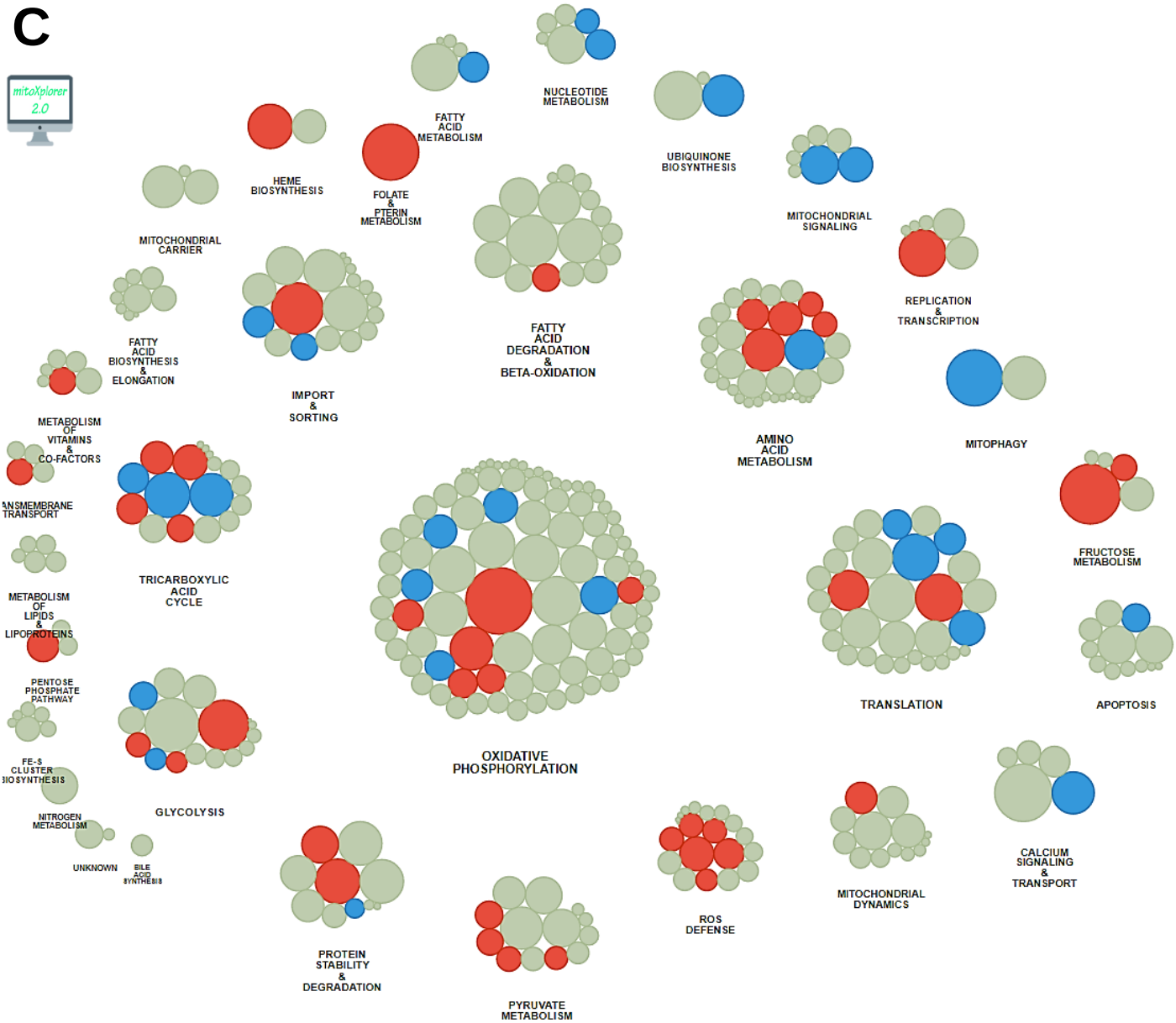

Figure S6

PROTEOME

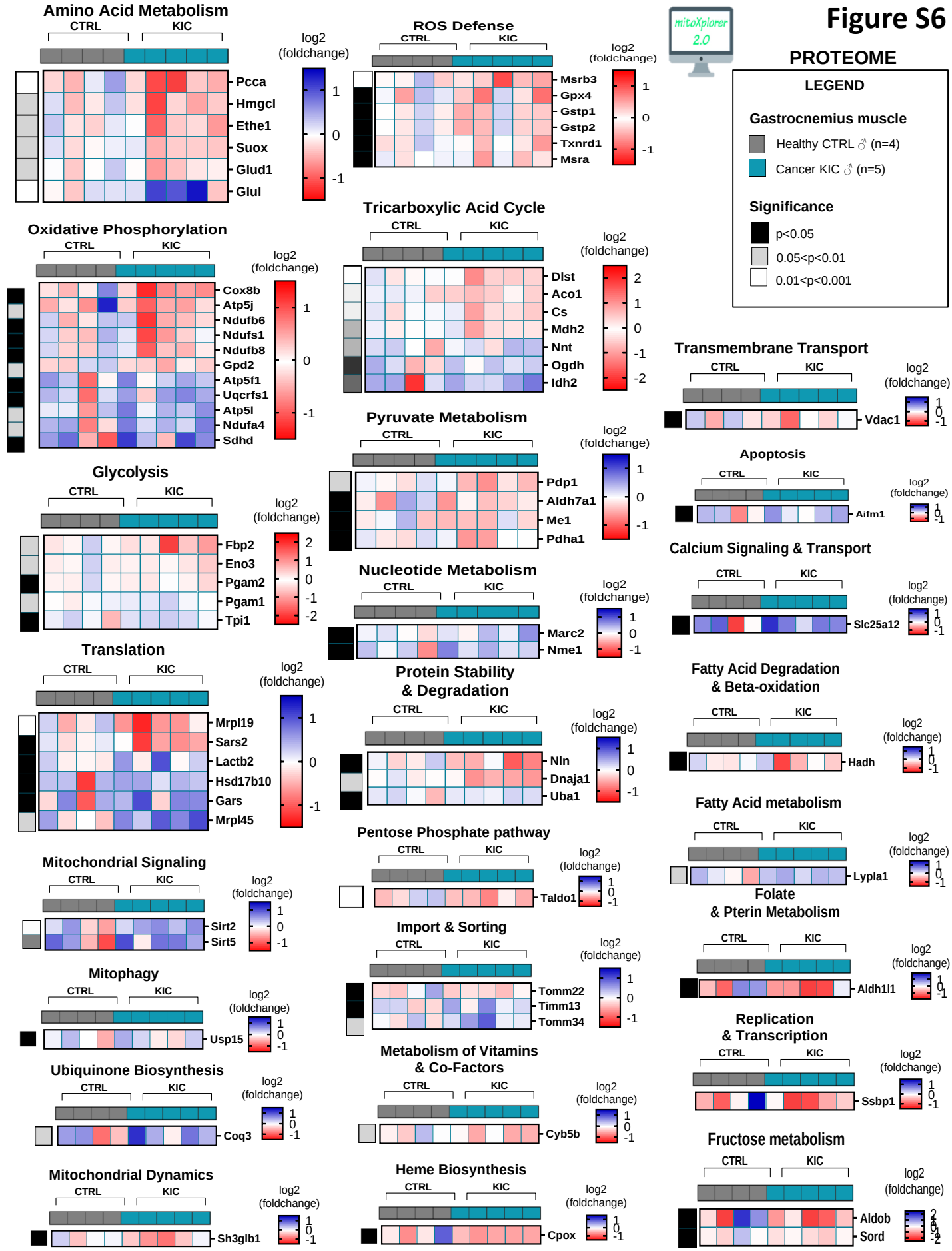

Figure S7

Common mitochondrial dysregulated pathways between transcriptome and proteome:

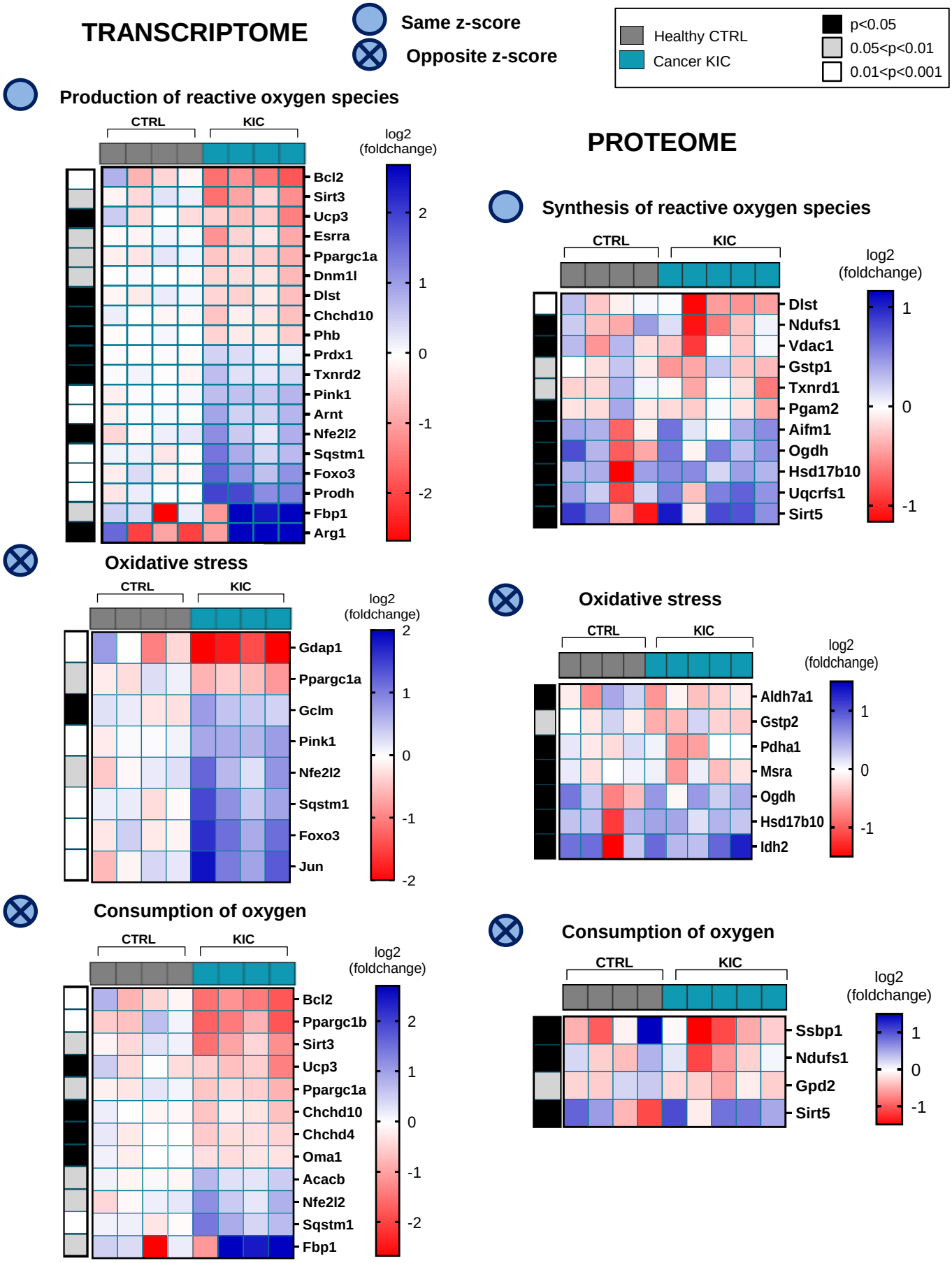

Figure S8

Common mitochondrial dysregulated pathways between transcriptome and proteome:

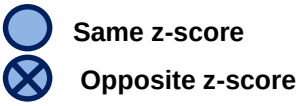

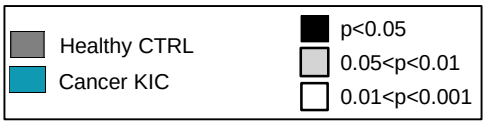

TRANSCRIPTOME

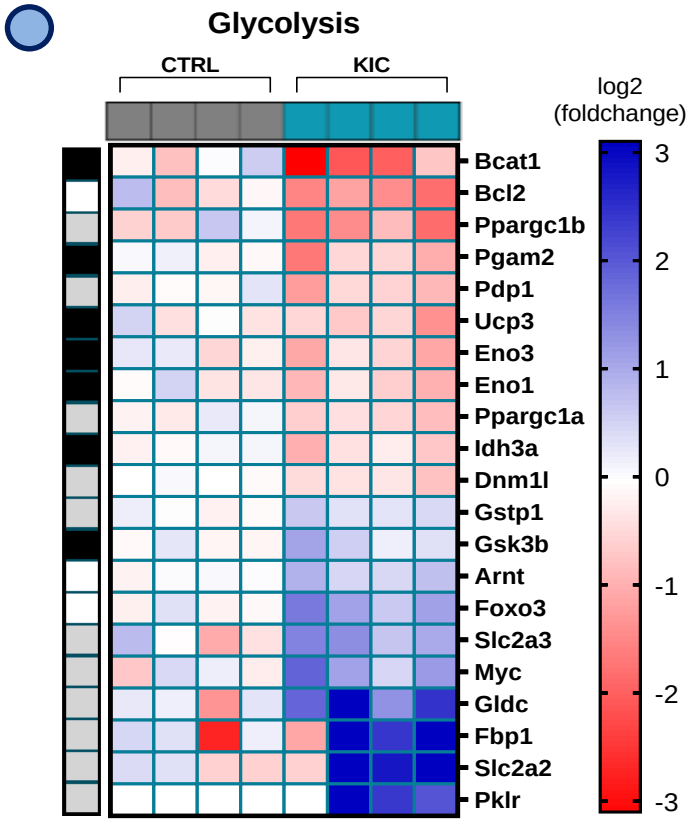

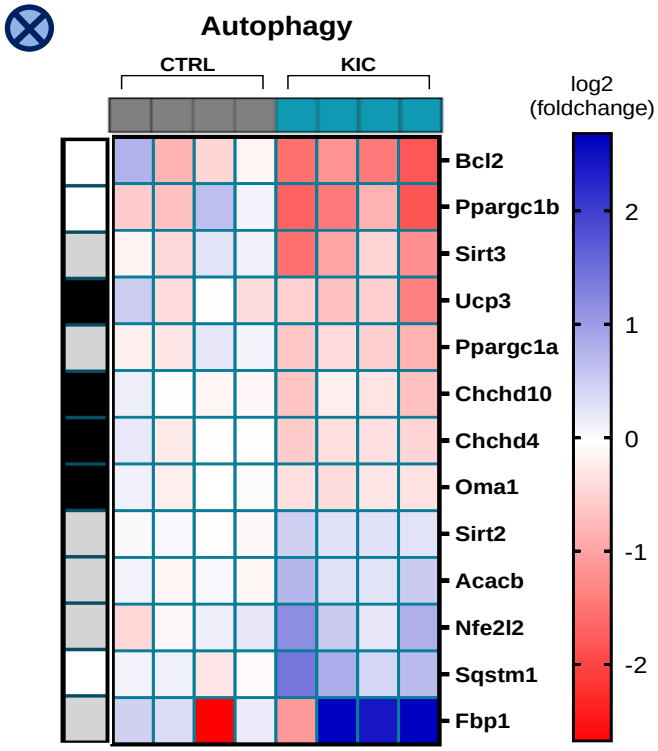

PROTEOME

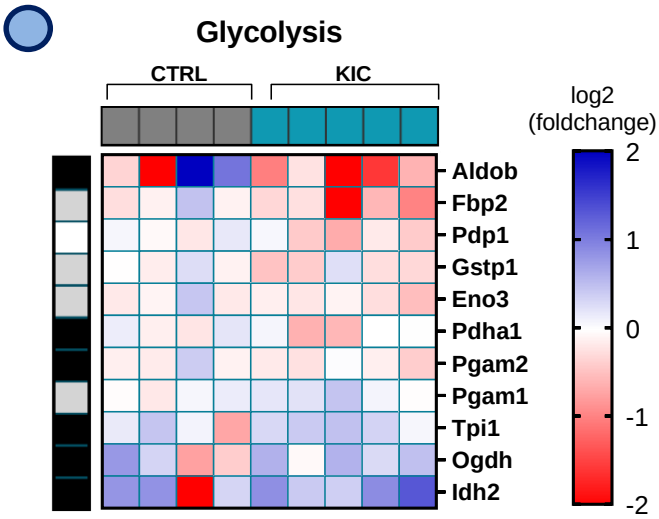

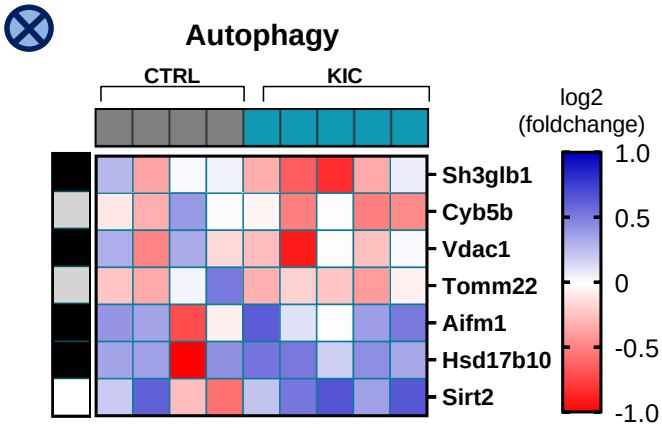

Figure S9
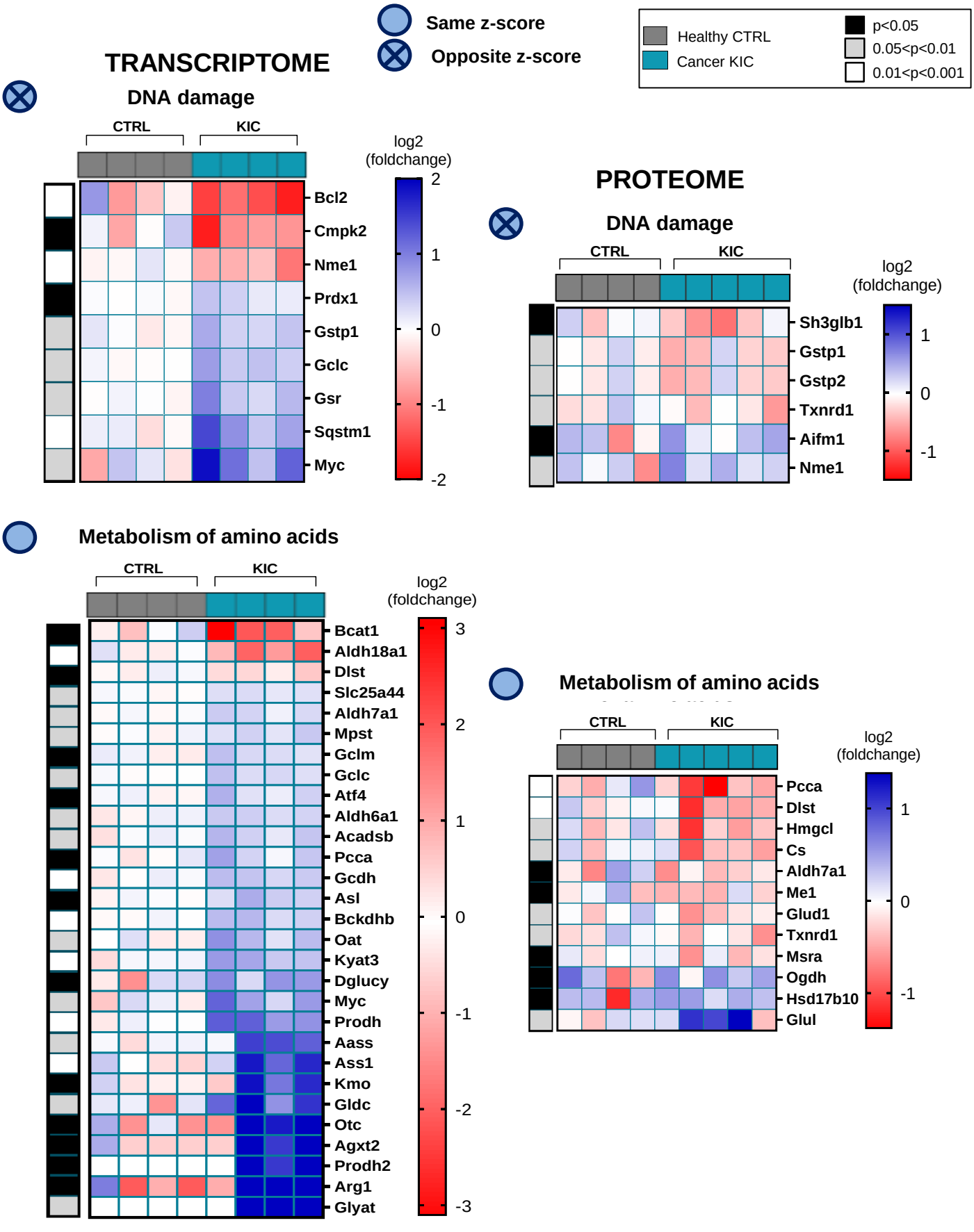
Common mitochondrial dysregulated pathways between transcriptome and proteome: